UNIVERSITY OF CALIFORNIA
Los Angeles

Oxide-Free Gadolinium Nanoparticles as MRI Contrast Agents

A dissertation submitted in partial satisfaction
of the requirements for the degree
Doctor of Philosophy in Biomedical Engineering

by

Yavuz Nuri Ertaş

2017

ABSTRACT OF THE DISSERTATION

Oxide-Free Gadolinium Nanoparticles as MRI Contrast Agents

by

Yavuz Nuri Ertaş
Doctor of Philosophy in Biomedical Engineering
University of California, Los Angeles, 2017
Professor Louis-Serge Bouchard, Chair

The Gd element and other rare-earth metals are notoriously difficult to use in chemical synthesis due to their high reduction potentials and aggressive reactivities with ambient oxygen, which almost always leads to the formation of oxides. The challenge in chemical synthesis limits the range of applications for rare-earth metals. The most important use of Gd at the moment is nanocrystals for technological applications. Herein, we report for the first time the successful production of size-controllable, solid core-shell oxide-free Gd metal nanocrystals. We have solved the long-standing problem of oxidation through a reduction process and appropriate capping. The manuscript describes the procedure and detailed characterizations of the process to ensure the highest quality of the produced particles. In particular, the nanocrystals displayed the largest saturation magnetization observed to date for nanocrystalline Gd metal. This value (206 emu/g at 2K) currently stands as the world record.

Another important application of Gd is contrast agent development for MRI. To this end, we have performed NMR relaxivity measurements to evaluate the performance of the nanoparticles as potential MRI contrast agents. Typically, Gd based nanoconstructs such as FDA approved Gd-DTPA chelates are T_1 MRI contrast agents; however, we demonstrate, for the first time, that pure Gd nanoparticles can also be used as state-of-the art T_2 contrast agents. World record

high values for transverse proton relaxitivity (r_2) of 232 $mM^{-1}s^{-1}$ per Gd atom and per-particle relaxivity (2.9 x 10^8 $mM^{-1}s^{-1}$) have been obtained, exceeding the current highest per-particle r_2 values. These results make our Gd nanocrystals the most promising MRI contrast agents for use in biomedical applications. For the first time, this puts MRI on par with positron emission tomography in terms of sensitivity to detection of a contrast agent.

We further developed the nanoparticles and we demonstrate record high saturation magnetizations for Gd nanoparticles, namely, 226 emu/g at 5 T. This magnetization is substantially higher than anything achieved to date. We have achieved such high magnetizations in a reliable and reproducible manner by controlling the crystallinity of the grown Gd nanofilm. The crystallinity of Gd is found to play an important role in the observed magnetization values. The higher magnetization is observed for nanoparticles that have a lower content of paramagnetic face-centered cubic (fcc) phase and greater content of ferromagnetic hexagonal close-packed (hcp) phase. Control over fcc and hcp content in the lattice was achieved by adjusting the deposition rate of Gd metal during the nanofabrication process. Our results indicate the remarkable influence of nanocrystallinity on the magnetism of Gd and the ability to control it.

Our novel fabrication technique, which overcomes the problems of current synthetic approaches to rare-earth nanoparticle synthesis through the careful optimization of capping and hydrogen reduction techniques, can also be applied to other rare-earth metals and alloys. This opens the door to fundamental studies on these materials at the nanoscale. It will also enable the realization of the full potential of rare-earth metals in industry.

The dissertation of Yavuz Nuri Ertaş is approved.

Dino Di Carlo

Jacob J. Schmidt

Yung-Ya Lin

Louis-Serge Bouchard, Committee Chair

University of California, Los Angeles

2017

to my family and future wife...

Table of Contents

List of Figures

List of Tables

Acknowledgments

I would like to thank all people, some of which I cannot even remember and mention their names, who contributed to my scientific knowledge and journey.

My family deserves a thanks as well for their patience and bearing my being far away from them for years.

My gratitude and thanks go to my classmates, collaborators, coworkers and colleagues, specifically to all Bouchard Lab members.

I also want to thank my advisor, Prof. Louis-S. Bouchard along with my committee members; Profs. Dino Di Carlo, Jacob J. Schmidt and Yung-Ya Lin.

I find it valuable to have several academic and non-academic people around me who share their views and feedback with me. Particularly, I enjoy the negative criticism which in my opinion is an opportunity to improve. I appreciate everyone who truthfully shows me my wrong sides, providing me a chance to become better.

Vita

2007	Başkent University, Turkey B.S. in Biomedical Engineering
2009	Bilkent University, Turkey M.S. in Materials Science and Nanotechnology
2011	University of California, Los Angeles M.S. in Biomedical Engineering

Publications

Effects of Cd vacancies and unconventional spin dynamics in the Dirac semimetal Cd_3As_2, Dimitrios Koumoulis, Robert E. Taylor, Jeffrey McCormick, Yavuz N. Ertaş, Lei Pan, Xiaoyu Che, Kang L. Wang, and Louis-S. Bouchard *The Journal of Chemical Physics*, **2017**, 147, 084706.

Aqueous Ligand-Stabilized Palladium Nanoparticle Catalysts for Parahydrogen-Induced ^{13}C Hyperpolarization, Jeffrey McCormick, Alexander M. Grunfeld, Yavuz N. Ertaş, Akash N. Biswas, Kristofer L. Marsh, Shawn Wagner, Stefan Glöggler, and Louis-S. Bouchard *Analytical Chemistry*, **2017**, 89, 7190-7194.

Controlled nanocrystallinity in Gd nanobowls leads to magnetization of 226 emu/g, Yavuz N. Ertaş, and Louis-S. Bouchard *Journal of Applied Physics*, **2017**, 121, 093902.

Surface ligand-directed pair-wise hydrogenation for heterogeneous phase hyperpolarization, S. Glöggler, Alexander M. Grunfeld, Yavuz N. Ertaş, Jeffrey McCormick, Shawn Wagner, and Louis-S. Bouchard *Chemical Communications*, **2016**, 52, 605-608.

Supercapacitor behaviors of polyaniline/CuO, polypyrrole/CuO and PEDOT/CuO nanocomposites, Murat Ates, Mehmet A. Serin, Ilker Ekmen, and Yavuz N. Ertaş *Polymer Bulletin*, **2015**, 72, 2573-2589.

Oxide-Free Gadolinium Nanocrystals with Large Magnetic Moments, Yavuz N. Ertaş, Nanette N. Jarenwattananon, and Louis-S. Bouchard *Chemistry of Materials*, **2015**, 27, 5371-5376.

High-throughput and label-free single nanoparticle sizing based on time-resolved on-chip microscopy, Euan McLeod, T. Umut Dincer, Muhammed Veli, Yavuz N. Ertaş, Chau Nguyen, Wei Luo, Alon Greenbaum, Alborz Feizi, and Aydogan Ozcan *ACS Nano*, **2015**, 9, 3265-3273.

A Nanoparticle Catalyst for Heterogeneous Phase Para-Hydrogen-Induced Polarization in Water, Stefan Glöggler, Alexander M. Grunfeld, Yavuz N. Ertaş, Jeffrey McCormick, Shawn Wagner, P. Philipp M. Schleker, and Louis-S. Bouchard *Angewandte Chemie International Edition*, **2015**, 54, 2452-2456.

Effects of multivariate linker substitution, metal binding, and reactor conditions on the catalytic activity of a Pd-functionalized MOF for olefin hydrogenation, Trenton Otto, Nanette N. Jarenwattananon, Stefan Glöggler, Jonathan W. Brown, Arek Melkonian, Yavuz N. Ertaş, and Louis-S. Bouchard *Applied Catalysis A: General*, **2014**, 488, 248-255.

CHAPTER 1

Introduction

1.1 Principles of MRI

Magnetic resonance imaging (MRI) is a non-invasive technique based on the magnetic fields of protons within the body, producing views of internal organs or tissues. MRI technique utilizes the principles of nuclear magnetic resonance (NMR), a spectroscopic technique used by scientists to obtain microscopic chemical and physical information about molecules, which was discovered by Felix Bloch and Edward Purcell independently in 1946, which brought them the 1952 Nobel Prize [1]. The technique was called MRI rather than nuclear magnetic resonance imaging (NMRI) because of the negative connotations associated with the word nuclear in the late 1970's. Initially, MRI was a tomographic imaging technique which used to generate an image of the NMR signal in a thin slice through the human body, however over time, it has become a volume imaging method [2]. After receiving the FDA approval for clinical use in 1985, MRI has become a major diagnostic tool in modern medicine and was adapted by hospitals around the world since then [3]. Magnetic resonance imaging has become one of the most important and evolved as a frontier method in medical diagnosis and biomedical research as it combines some of the most interesting principles of physics and some of today's most advanced technology. The need for invasive diagnostic procedures has been limited by the use of MRI and it is able to provide physiological information earlier in clinics. Today, in addition to anatomic detail and contrast, MRI also provides functional information which is useful in disease characteriza-

tion [4]. It also offers fast scan times, the capacity to produce excellent quality and high-resolution images and the avoiding of radiochemicals. Compared to other modalities, MRI has the highest spatial resolution and clinical potential, and can image structures in the millimeter scale without the use of ionizing radiation such as that used in X-ray and computerized tomograph (CT). MRI provides several advantages over other clinical modalities such as high spatial resolution, noninvasiveness, high anatomical contrast, high capacity of differentiating soft tissues without the use of ionizing radiation [5]. However, MRI suffers from low sensitivity compared to radionuclide methods such as positron emission tomography (PET) and single-photon emission computed tomography (SPECT).

The basis for MRI signal is the precession of water hydrogen nuclei within an applied magnetic field. It involves imaging of the proton, the positively charged spinning nucleus of hydrogen atoms because they are abundant in tissues containing water, proteins, lipids and other macromolecules [6]. The human body is composed of 70% water by weight. The water molecule contains two hydrogen protons, therefore our body is an ideal object for a MRI. A proton has a minuscule magnetic field due to an intrinsic property called nuclear spin and charge, which makes it behave like a compass needle in a magnetic field and aligns itself with respect to the field. According to quantum mechanics, atoms with an odd number of protons are designated a spin of $\pm\frac{1}{2}$ by which they intrinsically possess an associated magnetic moment and angular momentum. Under the presence of a strong magnetic field B_0, the magnetic moments of the atoms will tend to align along the B_0 field. The strength of the B_0 field is generally given in Tesla (T) unit. Along with the alignment of magnetic moments, the atoms also undergo a process known as *precession* about the induced magnetic field. Precession refers to rotation about an axis that is constantly changing; the effect can be visualized as the spinning of a top. The protons placed in a magnetic field start rotating around their axis at a frequency determined by a constant number and magnetic field

strength (Figure 1.1). This rotational motion is called magnetic resonance and is defined by the most essential equation of magnetic resonance, Larmor equation:

$$\omega = \gamma B_0 \tag{1.1}$$

where γ is the proton specific constant called gyromagnetic constant.

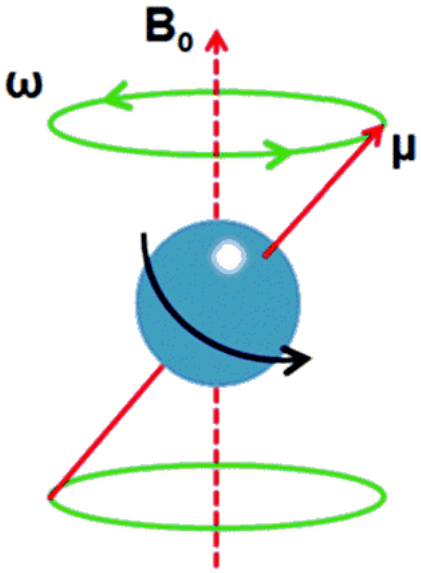

Figure 1.1: NMR spin precession

The protons placed in static field B_0 immediately start rotating (resonating) with ω at counterclockwise direction.

When radiofrequency (rf) pulses resonant at the Larmor frequency are introduced, the protons which are originally aligned with the external magnetic field absorb the rf energy and change their orientation. After this excitation, the protons start to release the absorbed energy which is called the relaxation process. This process in which the protons return to the original aligned state can be utilized to produce an image which represents a display of spatially localized signal

intensities [7]. The relaxation happens on two different time scales: The magnetization perpendicular to the magnetic field (the transversal magnetization) often decreases relatively rapidly, while it can take considerably longer to recover the magnetization along the field (the longitudinal magnetization). The longitudinal magnetization (M_z) approaches equilibrium M_o on a timescale T_1 whereas the transversal magnetization (M_{xy}) decreases exponentially on a timescale T_2. During the T_1 relaxation process, the net magnetization (M) returns to its initial maximum value (M_o) parallel to B_0 whereas during the T_2 relaxation process, the transverse components of magnetization (M_{xy}) decay.

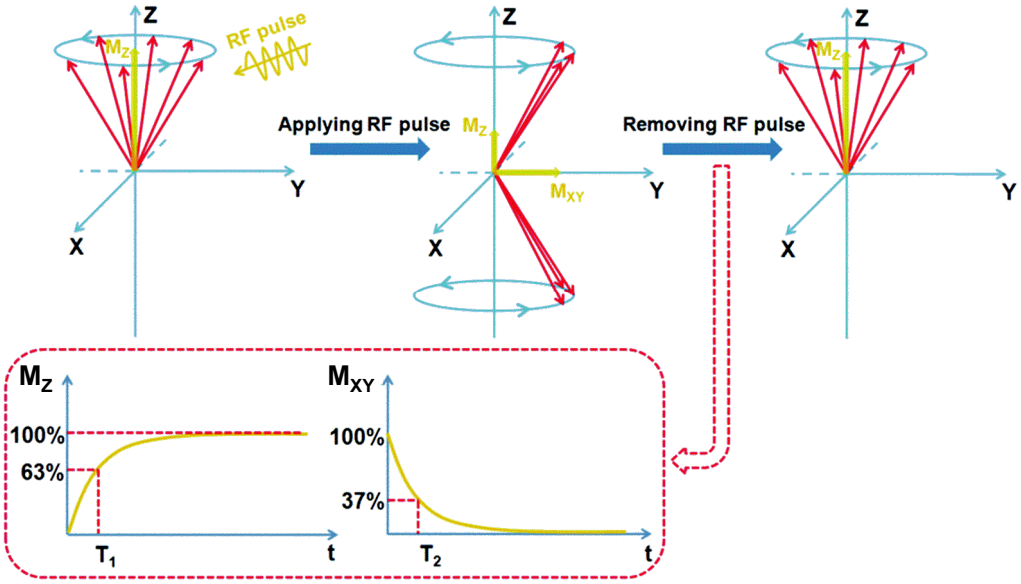

Figure 1.2: NMR relaxation times

Schematic illustration of the mechanisms of MRI. Protons precess under an external magnetic field B_0. After the introduction of the RF pulse, protons are excited, with relaxation occurring following removal of the RF pulse. And the graphical representation of T_1 relaxation and T_2 relaxation. T_1 relaxation is the process by which the net magnetization (M) returns to its initial maximum value (M_o). M_{xy} component of magnetization is lost in T_2

relaxation. (Reproduced from [8])

T_1 relaxation is also known as spin-lattice or longitudinal relaxation. T_1 can be viewed as the time required for the z-component of M to reach (1-1/e) or about 63% of its maximum value (M_o) (Figure 1.2). As the longitudinal component of M (M_z) grows toward M_o, the energy of the spin system decreases because more spins prefer the lower energy, therefore energy must leave the T_1 relaxation to occur. This is why T_1 relaxation is also called thermal relaxation. T_1 depends on tissue composition, structure and surroundings as it is related to the exchange of thermal energy, which is transferred over from the protons to the surroundings, the lattice.

T_2 relaxation is also known as spin-spin or transverse relaxation. T_2 is the time required for the transverse magnetization to decrease to approximately 37% (1/e) of its initial value (Figure 1.2). T_2 relaxation happens when protons go out of phase, which has two causes: inhomogeneities of the external magnetic field, and inhomogeneities of the local magnetic fields within the environment.

T_1 and T_2 relaxation times need to be shortened in order to obtain better image contrast. For this purpose, contrast agents have been developed for the last several decades. The contrast agents which shorten the T_1 time are called T_1 contrast agents, similarly those of which shorten the T_2 are called T_2 contrast agents.

1.2 MRI Contrast Agents

Although MRI has many advantages over other imaging modalities, there remains the issue of insufficient contrast between the healthy and diseased tissues due to relatively small structural differences, and results in a correspondingly low apparent MRI sensitivity for identifying the associated abnormalities [9]. Thus, MRI

sensitivity needs to be improved. In order to overcome this limitation, contrast agents have been used to increase the signal contrast between the tumor tissue and normal tissue. MRI contrast agents are chemical compounds that are able to alter the relaxation times of water protons in tissues where they are distributed [10]. This in turn leads to remarkable improvements in medical diagnoses, as they facilitate higher sensitivity and specificity and better tissue characterization [11]. Contrast agents can be divided into two groups depending on whether they cause changes in either T_1 or T_2 relaxation rates of the water protons, these being known as positive or negative agents respectively. The ability of an agent to affect T_1 and T_2 is characterized by the concentration-normalized relaxivities r_1 and r_2 respectively. These parameters refer to the amount of increase in $1/T_1$ and $1/T_2$ respectively, per millimole of agent, and are normally quoted as a rate ($\mathrm{mM}^{-1}\mathrm{s}^{-1}$). The values are used to determine the efficiency of a contrast agent, and they consist of contributions from both inner sphere and outer sphere relaxation mechanisms.

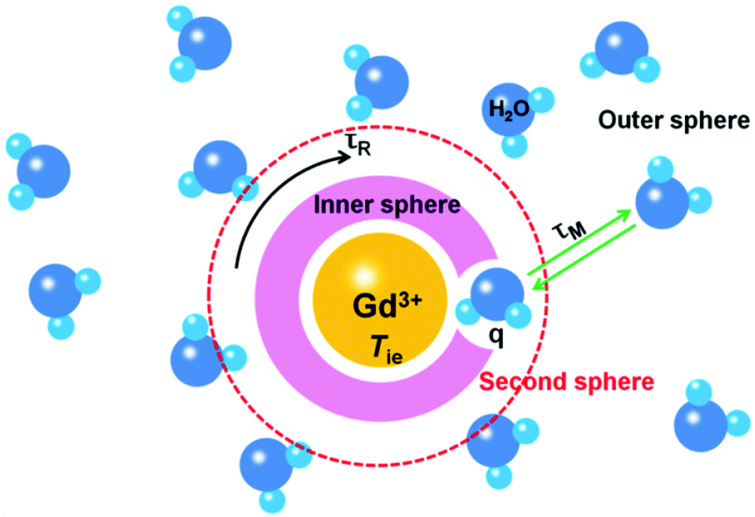

Figure 1.3: Inner and outer sphere effect

Inner sphere effect occurs when the water molecules directly coordinate to the magnetic ion at the core and outer sphere effect utilizes the bulk water molecules diffusing in the near environment.

There are several factors affecting the relaxivity efficiency of the magnetic molecule (Figure 1.3). The main region in close vicinity of the magnetic matter that increases relaxivity efficiency could be divided into an inner sphere and outer sphere, where water molecules directly coordinate to the magnetic ion and bulk water molecules diffusing in the near environment, respectively, are both influenced by the magnetic ion. In some cases, the second sphere where water molecules are hydrogen bonded to the chelating unit is taken into account. In the region of the inner sphere, the main parameters include longitudinal and transverse electronic relaxation times and the hydration number of water molecules (q). Another critical parameter is the rotational correlation time τ_R or the time needed for reorientation of the metal-proton vector, and a higher τ_R means slower molecular tumbling, leading to the improvement of proton relaxivity. The parameter τ_M refers to the residence time of water molecules in the inner sphere, which is favorable for proton relaxivity in the case of fast water exchange [8]. Contrast agents can display relaxivity even when there is no water molecule binding to the magnetic core which means there is no water in the inner coordination sphere, then the relaxivity must come from outer sphere contribution.The outer sphere relaxation arises due to diffusion of water molecules in the bulk near to the magnetic core. The electronic relaxation time of the magnetic core and the distance of the closest approach of solvent and solute and the sum of their diffusion coefficients play role in this case [1].

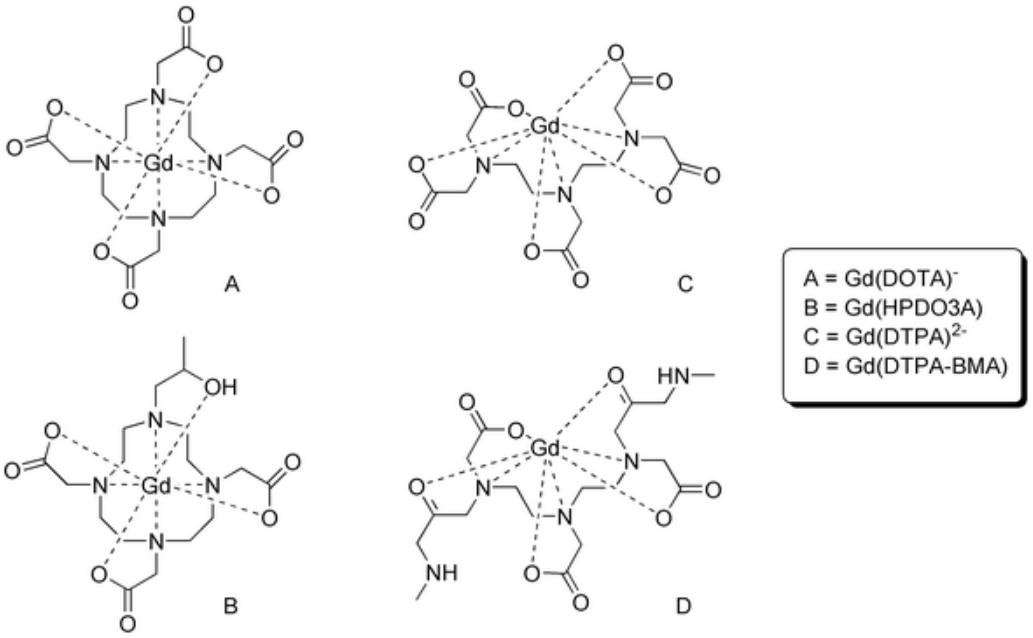

Figure 1.4: Chelated Gd^{+3} molecules

Commercially available and FDA approved chelated gadolinium-based contrast agents.

Positive contrast (T_1) agents commonly utilizes the paramagnetic materials, mainly those based on metal ions with large numbers of unpaired electrons, such as Mn^{+5} (5 unpaired electrons), and Gd^{+3} (7 unpaired electrons). The vast majority of positive contrast agents are based on gadolinium ion, however, since the gadolinium ion possesses an ionic radius close to that of calcium ion but a higher positive charge, proteins cannot recognize them and Gd^{+3} would quickly bind to Ca^{+2} channels and other proteins that require Ca^{+2} such as calmodulin, calsequestrin and calexitin [12]. As a result, free gadolinium ions are toxic in biological systems and cannot be administered to a patient in their aqueous form. To suppress the potential toxicity, the gadolinium ion is usually bound by a strongly coordinating ligand for clinical examinations. This is called chelation. Figure 1.4 shows some of the FDA approved chelated Gd contrast agents. Besides chelation, T_1 contrast agents can be administered in different forms such as loading

the paramagnetic ions in polymeric micelles, nano-hydrogels, mesoporous silica nanoparticles, liposomes polymersomes and dendrimers [13]. Oxide compounds of the magnetic ions such as Gd_2O_3 and MnO are also act as T_1 agents [8]. T_1 contrast agents produce an image being brighter within areas where the agents are taken up, due to brightness being a function of T_1.

Negative contrast (T_2) agents influence the signal intensity by shortening transverse relaxation (T_2), thereby producing darker images as high T_2 results in increased brightness of the images. Negative contrast agents are commonly formed of superparamagnetic materials such as iron oxide nanoparticles. To produce efficient T_2 contrast agents, the magnetic properties of the nanoparticles need to be controlled through the designed control of the intrinsic material properties, such as material composition and crystal structure, as well as extrinsic factors, such as size and shape. T_2 contrast agents include superparamagnetic, paramagnetic and ferromagnetic materials. The most commonly used T_2 contrast agent is superparamagnetic iron-oxide nanoparticles. In metallic nanoparticles, such as Co, Fe, FeCo and FePt, all the magnetic spins align parallel to the external field; as a result, they typically have higher magnetic moments than those of ferromagnetic or magnetic ceramic nanoparticles. The metallic nanoparticles result in a larger effect on proton relaxation, providing improved MRI contrast and allowing for smaller magnetic nanoparticles core use without compromising sensitivity.

CHAPTER 2

Oxide-Free Gadolinium Nanocrystals with Large Magnetic Moments

Lanthanides exhibit unique magnetic and optical properties that are useful in modern technological applications. Through their unpaired $4f$ spins, six lanthanides ($Z = 64 - 69$) exhibit larger magnetic moments per atom than iron [14]. Nanoparticles of gadolinium (Gd), the most abundant member of the rare-earth metals, are of particular interest for applications to biomedical imaging [15–24], neutron-capture therapy [25–29], theranostics [30], temperature-sensing [31] and magnetic refrigeration [32–35]. In the latter case, heat is removed from a medium by exposing it to a changing magnetic field. The best performance has been achieved with Gd and its alloys, because of a high Curie temperature [36] and magnetic moment [35]. As the particle size decreases, heat exchange improves and eddy current losses are reduced.

The production of nanoparticles with optimal properties is challenging due to the tendency of Gd to oxidize rapidly. Chemical synthetic routes lead to the formation of Gd oxides, because of the high reduction potential and aggressively reactive nature of Gd. The oxide forms inherit magnetic properties that are suboptimal compared to pure Gd, in particular, a substantially reduced magnetization [37]. Other lanthanides also present the same issue of oxide formation, severely limiting their uses in industry and implying that the potential of rare-earth metals has not yet been fully realized. Synthetic approaches have included the use of multilayer precursors, alkalide reduction, gas-phase, and arc-discharge methods [38–44]. In

spite of these efforts, there exists only one report describing the synthesis of stable Gd nanoparticles, namely a core-shell Gd@Au structure [45]. Good size control and uniformity across a wide range of particle sizes has not yet been demonstrated. Even a glove box environment fails to completely prevent oxidation of the Gd core.

Herein, we report on the production of gadolinium nanoparticles that are completely oxide-free, stable and whose size can be well controlled. Gadolinium was selected for this work due to its prevalent use as a building block for magnetic resonance imaging (MRI) contrast agents. Chelated Gd^{3+} ions, which are already FDA-approved for use in clinical MRI, act as T_1 contrast agents due to the rapid exchange of water protons in the vicinity of the paramagnetic ion. Gadolinium-based oxide nanoparticles, which have been the subject of recent studies [15–24], as potential MRI contrast agents, act as T_2 agents due to the dominant contribution from the static magnetic moment. There have been no reports on the MRI properties of pure (i.e. oxide-free) Gd nanoparticles, presumably because of the difficulty of synthesizing such particles.

The approach we developed is based on nanofabrication. Nanofabrication is an alternative to chemical synthesis that is largely ignored for biomedical applications because the yields are low, the nanopatterning steps are costly and the wafers are often not reusable, thereby limiting scalability [46]. For example, the growth of nanoparticles on nanopillar arrays involves etching of the silicon wafer to the point where the same costly substrate can no longer be re-used [47]. We instead describe the use of nanosphere lithography [48, 49], which enables indefinite recyclability with proper wet cleaning of the substrate surface. When combined with a hydrogen reduction technique, the end product is a core-shell Gd nanocrystal ($Gd@SiO_2$) that is oxide-free, surfactant-free, stable, monodisperse and size-tunable. We have chosen silica for the shell layer for biocompatibility; the nontoxicity of silica nanoparticles is well documented [50–52]. We demonstrate broad tunability of the particle size while maintaining a remarkably narrow

size distribution ($< 5\%$). The nanoconstructs displayed the highest magnetization measured to date for Gd nanoparticles, approximately 30% higher than the highest magnetization reported previously [45]. With biomedical applications in mind, NMR relaxivity measurements were performed to evaluate the performance of the nanoparticles as potential contrast agents for MRI. An unexpectedly high transverse proton relaxivity was measured, which is the highest value reported for any MRI contrast agent to date; this makes it the most promising T_2 based MRI contrast agent.

2.1 Experimental Detail

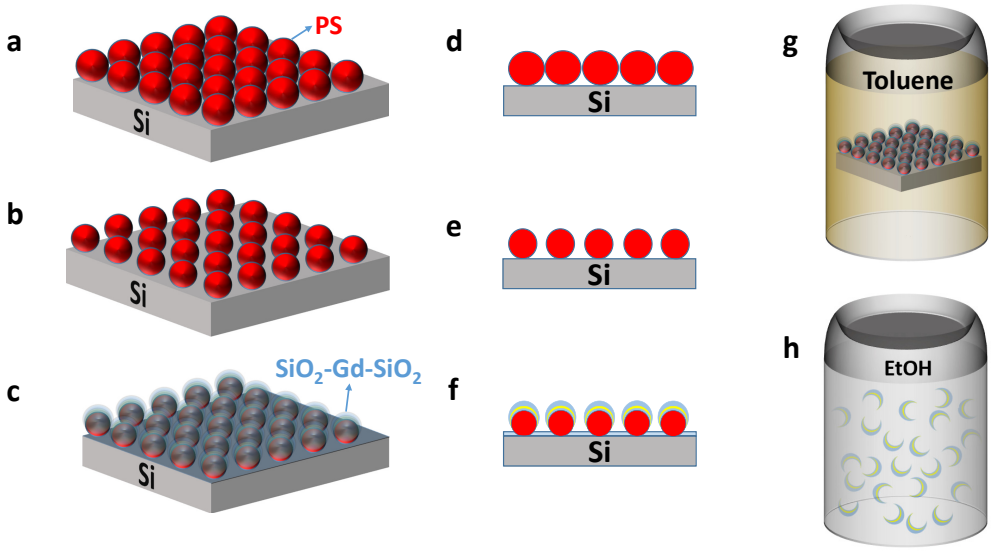

Figure 2.1: Nanofab process

Schematic of the nanofabrication process. a) Monolayers of polystyrene nanospheres are formed on silicon wafer pieces used as sacrificial templates. b) Spacings have been generated between the nanospheres by using oxygen reactive ion etching to etch the polystyrene. c) Layers of 10 nm SiO_2, 10 nm Gd and 20 nm SiO_2 were sequentially electron-beam evaporated onto the substrate. d-f) 2-D view of the process flow described in (a-c). g) Silicon wafer pieces with the patterned structures are immersed into a glass tube containing toluene

and placed in an ultrasonication bath for 4 hours. The toluene etches away the polystyrene, leaving the nanobowls suspended in solution. h) The solution is rinsed by centrifugation 3 times and the nanobowls are transferred to an ethanol (ETOH) solution for future use and characterization.

The nanolithography fabrication process we developed utilizes monolayers of polystyrene nanospheres as the template for metal deposition. Silicon wafer pieces were spin-coated with a monolayer of polystyrene nanobeads of 300 nm diameter (PS300NM Magsphere Inc., CA). In order to achieve a high surface coverage of nanospheres, the parameters of the spin-coating process have been optimized. The diameters of the polystyrene nanospheres were adjusted by O_2 reactive ion etching (RIE) to the desired size. Layers of 10 nm SiO_2, 10 nm Gd and 20 nm SiO_2 were electron-beam evaporated onto the 15° tilted substrates to create Gd@SiO_2 nanobowl-shaped structures (Figure 2.1). The structures were released by the sonication of substrates in a toluene suspension. The toluene etches away the polystyrene nanobeads, leaving the deposited structures freely suspended in solution. The nanobowls are collected by centrifugation and suspended in ethanol for future use.

There are two ways to adjust the particle size. The first approach is to adjust the etching parameters whereas the second approach is to use nucleation sites on nanospheres of different sizes. In both cases, the nanofabrication process produces a black powder. No change in the color of the product was observed upon exposure to ambient air over a time period exceeding a month or keeping the particles in ethanol solution and drying back again, which indicates that the particles are chemically air-stable. In contrast, bare Gd nanoparticles without a protective shell layer rapidly react with ambient air, forming a white Gd_2O_3 powder, which in turn reacts with water, losing stability and shape. When combined with glancing angle deposition, the monolayer templates generate high-quality,

bowl-shaped nanoparticles. The bowl shape results in the sealing of the magnetic core layer (Gd) as otherwise, ambient oxygen can diffuse into the core layer through the edges, oxidizing Gd to Gd_2O_3. The morphology of the nanostructures was characterized by scanning electron microscopy (SEM, JEOL JSM 7500F) and transmission electron microscopy (TEM, FEI CM120). Further detailed characterization of the core/shell nanoparticles was performed by high-resolution TEM (HRTEM) using a FEI Titan S/TEM (300 kV) instrument. Quantitative elemental EDX (energy dispersion x-ray) analysis of the nanoparticles was per-formed using spatially resolved EDX spectroscopy.

2.2 Results and Discussion

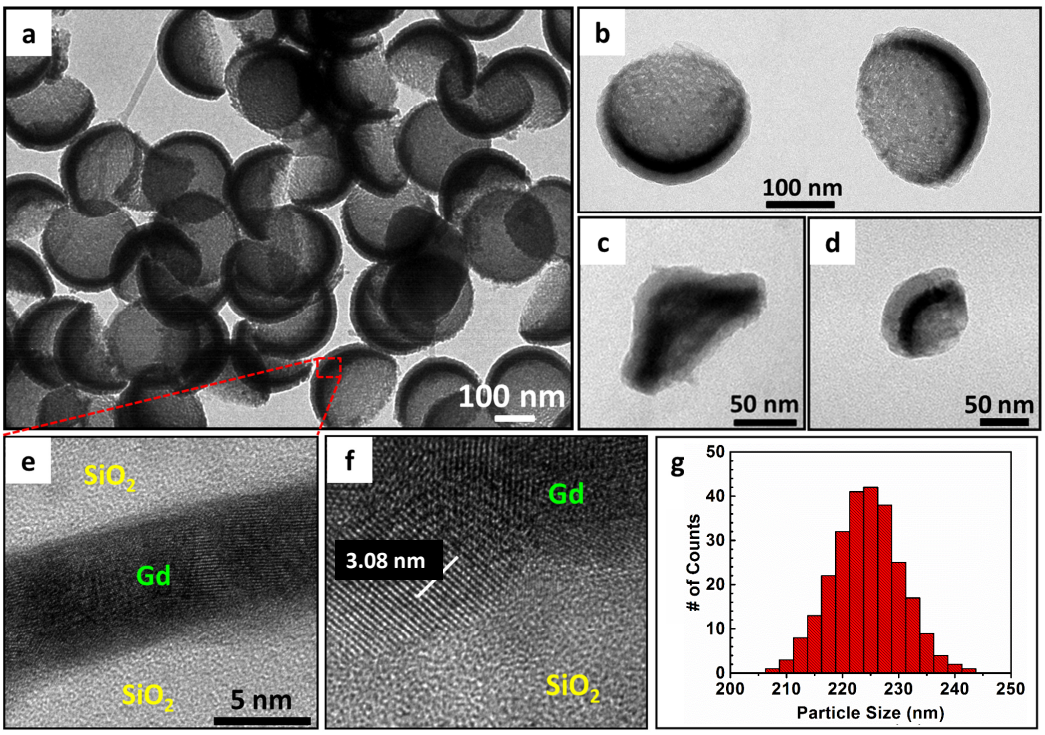

Figure 2.2: TEM analysis

TEM micrograph of a) nanobowl-shaped Gd@SiO_2 particles. b) 225 nm diameter nanoparticles. c) 120 nm diameter nanoparticles. d) 80 nm diameter nanoparticles. e) HRTEM

of core-shell layers. Amorphous SiO_2 and polycrystalline Gd layers are observed. f) HRTEM of silica and gadolinium layers. The measured crystal direction matches with the d-spacing of (111) plane of fcc cubic Gd. g) Histogram of Gd@SiO_2 nanoparticles (N=258 particles, largest dimension was measured by TEM).

The TEM image of the obtained nanoconstructs (Figure 2.2) shows that the product consists of highly uniform, bowl-shaped particles. The SEM image (Figure 2.3a) also reveals similar characteristics. The core-shell structure is depicted in Figures 2.2b,c,d where the light gray layer corresponds to the capping SiO_2 layer whereas the darker shades represent the Gd layer located in the core of the nanoconstruct (middle layer). The darker contrast is a consequence of the higher atomic number of Gd compared to SiO_2. The nanoconstructs of Figures 2.2b and 2.3b have a diameter of 225 nm. We demonstrate size tunability with smaller nanoparticles with a diameter of 120 nm (Figures 2.2c and 2.3c) and 80 nm (Figure 2.2d) with a total layer thickness of 40 nm (in order: 10 nm SiO_2, 10 nm Gd, 20 nm SiO_2) for both cases. The shape, size uniformity and structural stability of these smaller nanoparticles are found to be similar to those of the larger nanoparticles, as seen in Figures 2.2b,c,d. To confirm the nature of the core-shell structures, we have cross-sectioned the nanoconstructs using focused ion beam (FIB) milling followed by HRTEM imaging and elemental analysis. To prevent the oxidation of the core layer after the FIB process, the samples were kept in a vacuum box.

The results, which reveal the exact composition of each layer by elemental analysis (Figure 2.4), confirm the SiO_2-Gd-SiO_2 core-shell structure. The real-space HRTEM micrograph of Figure 2.2e following the FIB process confirms via electron-beam attenuation the nature of the core-shell structure, which consists of a Gd layer sandwiched between two amorphous SiO_2 layers. The polycrystalline character of the Gd layer is confirmed by real-space HRTEM (Figure 2.5), x-ray

diffraction (Figure 2.6b) and diffraction-mode HRTEM (Figure 2.2e).

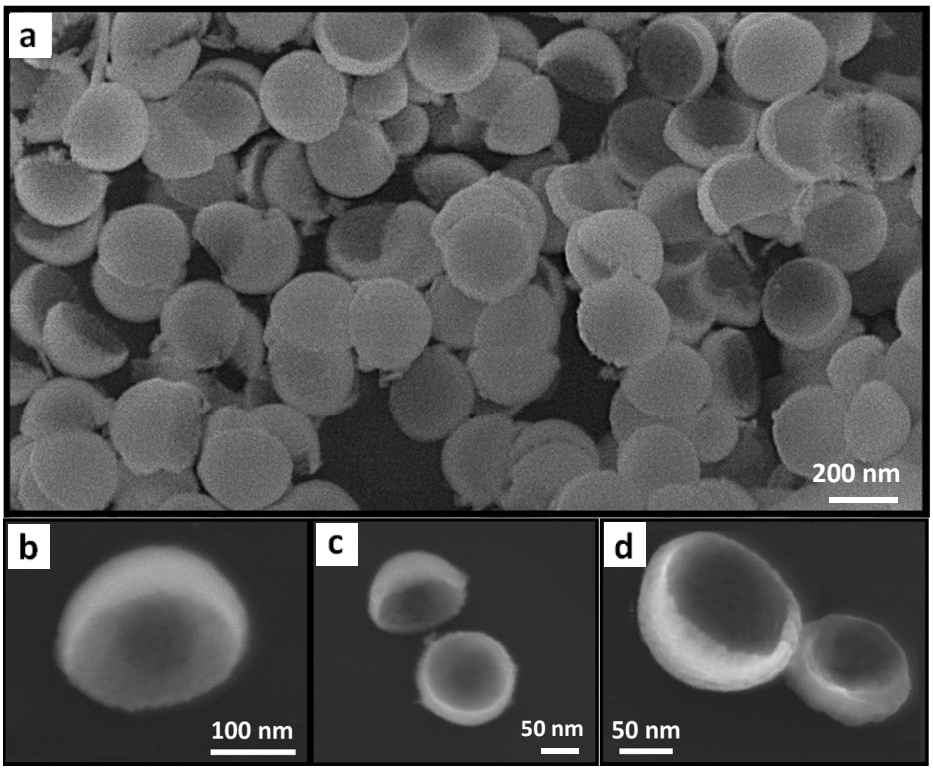

Figure 2.3: SEM analysis

a) SEM of randomly distributed Gd@SiO_2 nanoparticles. b) SEM of 225 nm nanoparticle. c) SEM of 120 nm nanoparticles. d) SEM of 225 nm and 120 nm particles shown together in the same image for size comparison purposes.

To determine the particle size distribution, the diameters of 258 particles were individually measured from HRTEM digital images. The resulting histogram is shown in Figure 2.2g. For the particles we have been referring to as "225 nm diameter particles", the average size was found to be 224±6 nm, implying that the product is highly monodisperse ($< 5\%$ variability). This remarkably uniform size distribution is a clear advantage of the nanofabrication process compared to chemical synthesis, which leads to higher size variability, especially for large

particles [53]. The electron beam deposition system enables the control of layer thickness in the Angstrom level.

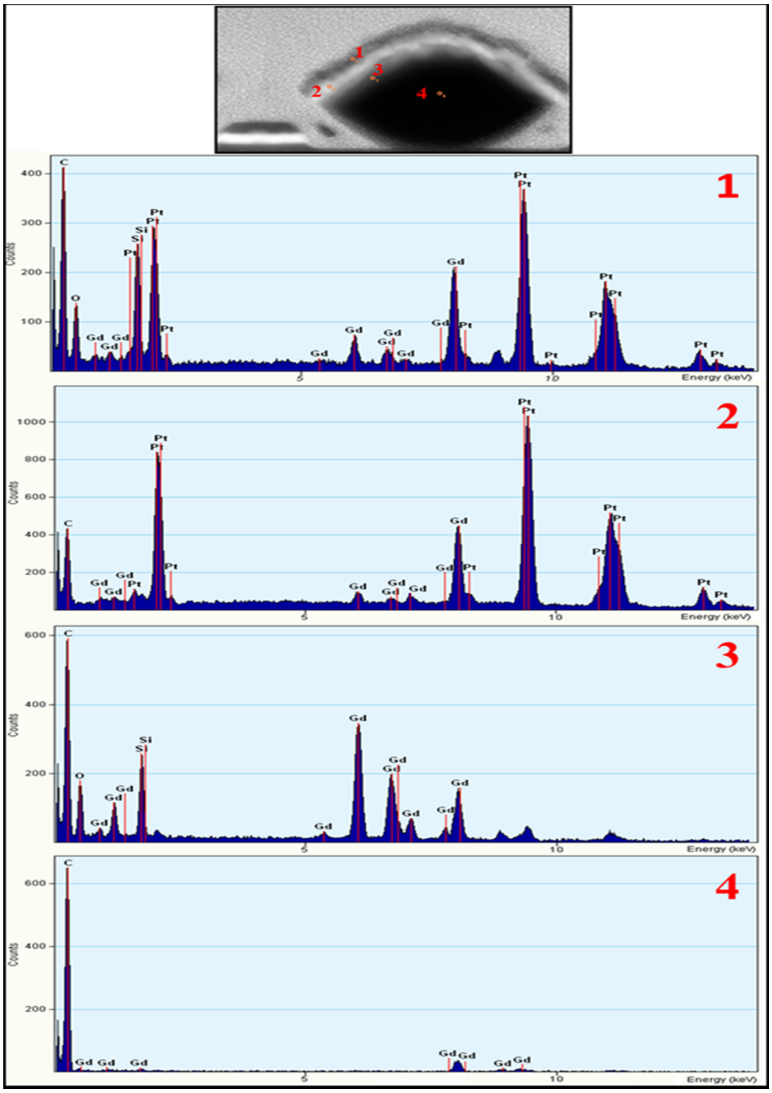

Figure 2.4: Elemental analysis

Top TEM image refers to the structure after it is sectioned by the FIB process. Spectra of 1, 2 and 3 refer to top (SiO_2), middle (Gd), bottom (SiO_2) layers respectively. Spectrum 4 refers to polystyrene nanosphere. Pt peaks originate from the platinum coating process during the FIB milling.

Figure 2.4 shows the elemental analysis of a nanoparticle after it is sectioned by the FIB process. Spectrum (1) shows the top SiO_2 layer whereas spectrum (3) shows the bottom SiO_2 with the corresponding peaks labeled. Spectrum (2) is the Gd layer. Spectrum (4) is the polystyrene template where plenty of carbon is detected due to its organic nature. The Pt peaks in the spectra arise from the FIB process as a layer of platinum is deposited during the sectioning process.

Figure 2.5: HRTEM analysis

Diffaction-mode HRTEM micrograph showing the polycrystalline behavior of the nanostructure.

High resolution TEM is used to obtain the data in Figure 2.5 which shows the diffraction pattern of the nanostructures. This indicates that nanostructures are in polycrystalline form.

Powder x-ray diffraction (PXRD, Bruker D8 Discover) analysis of the nanocrystals revealed that the structure is mostly composed of cubic Gd domains with cell

parameter $\alpha = 0.540$ nm (Figure 2.6a). A few small peaks were also observed which correspond to cubic Gd_2O_3 (JCPDS: 88-2165). The presence of oxide elements could originate from Gd regions that oxidize during the metal deposition step in spite of the 10^6 mtorr vacuum conditions. Gd is known to be extremely reactive to oxygen, even in the presence of trace amounts of oxygen. Thus, even under high vacuum conditions oxide formation is still prevalent. Nonetheless, we note that the observed Gd_2O_3 peaks are weak compared to the amount of oxide that would be obtained by chemical synthetic approaches [45].

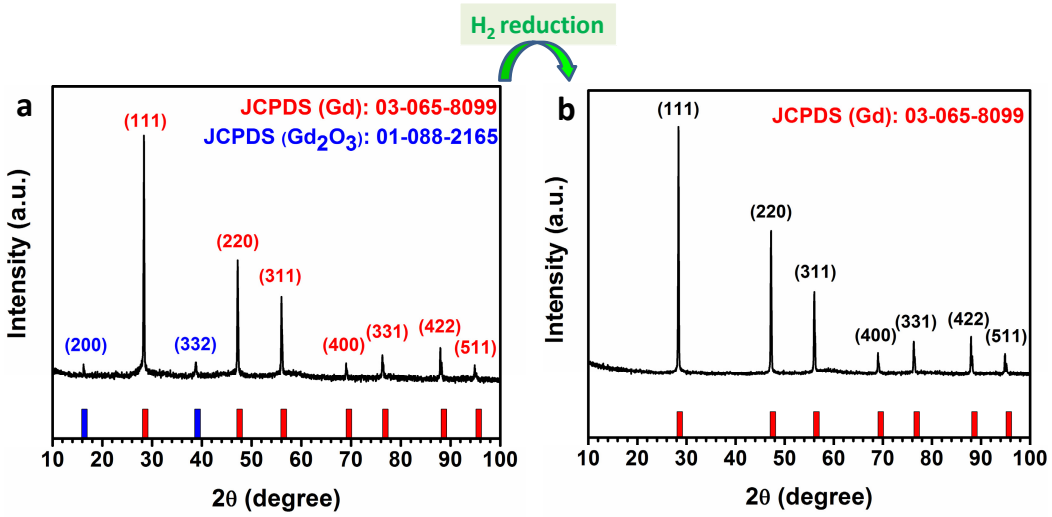

Figure 2.6: Elemental analysis

a) Powder XRD of the product before hydrogen reduction where mainly a gadolinium crystal pattern has been observed along with small peaks corresponding to gadolinium oxide. b) Powder XRD of the final product (after hydrogen reduction), confirming the fcc cubic Gd polycrystalline structure. The spectrum does not display any peaks attributable to Gd_2O_3, meaning that the core layer is entirely reduced to polycrystalline Gd metal after the H_2 reduction process.

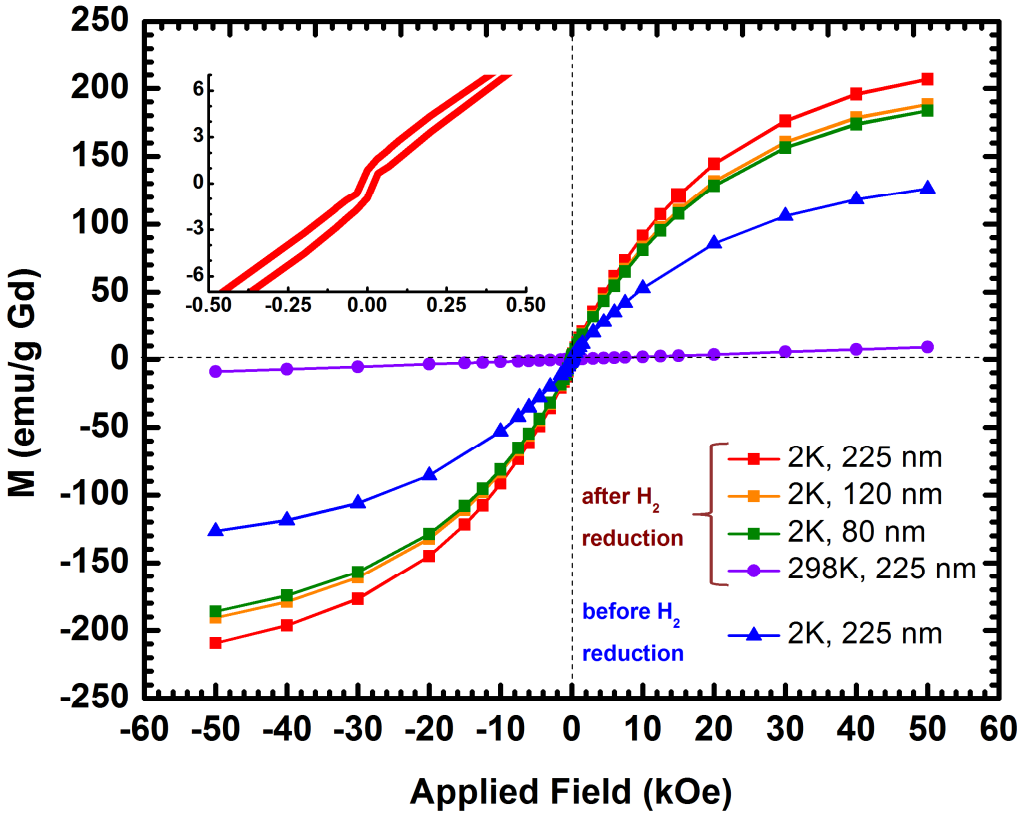

Figure 2.7: M-H curve

Magnetization measurements (M-H curve) for Gd@SiO_2 nanoparticles at 2 K after hydrogen reduction (squares, ■, ■,■), at 2 K before hydrogen reduction (triangles, ▲) and at 298 K after hydrogen reduction (circles, ●). Increasing particle size from 80 nm (■) to 225 nm (■) yielded higher peak magnetization values. We also note the improved magnetic properties after hydrogen reduction (■ vs ▲). Inset: Magnetic hysteresis after hydrogen reduction.

To create a more stable particle with a stronger magnetic phase, the oxide in the Gd layer must be completely removed. To achieve complete reduction of the gadolinium oxide regions, we modified a previously developed hydrogen reduction technique [54] in which hydrogen gas was used to reduce iron oxide to iron. In our case, the particles were subjected to a flowing gas mixture of H_2 and N_2 (9:1) at 600 °C for 5h. This process capitalizes on the high permeability of

SiO_2 layers to H_2 gas, which permits diffusion of the hydrogen gas through silicon dioxide layers. Once inside the layer, the H_2 gas can reduce the Gd oxide core and promote the formation of face-centered cubic (fcc) Gd nanocrystals. Although the formation of fcc cubic structure is promoted, what we observe in experiments is a polycrystalline Gd core (see PXRD pattern, Figure 2.6b). No peaks attributable to Gd_2O_3 were observed, implying that the core layer was entirely reduced. The observed d-spacing of 0.308 nm (Figure 2.2f) corresponds to the (111) plane of the fcc Gd structure where $d = 0.311$ nm (JCPDS: 65-8099). The complete reduction of oxidized regions can also be observed in the HRTEM EDX spectra (Figure 2.4) of the core layer, which failed to reveal any oxygen peaks.

The magnetic properties of the Gd@SiO_2 nanoconstructs were investigated by SQUID magnetometry (MPMS V XL Quantum Design) using external fields up to 5 T and temperatures in the range 2–298 K (Figure 2.7). M-H curves displayed a hysteresis effect at 2 K with a small coercive field of 20 Oe, indicative of a soft ferromagnetic state. In these nanoparticles, saturation is not reached at 5 T, likely because of the polycrystalline nature of the nanocrystals (see TEM images of Figure 2.2) leading to a distribution of easy axis orientations. In the discussion below, we therefore use the term peak magnetization instead of saturation magnetization. The peak magnetization of the 225 nm diameter Gd@SiO_2 particles at 2 K was 206 emu/g Gd, which is the highest value reported to date for any gadolinium nanoparticles. This value is significantly larger than the previously reported highest value of 156 emu/g [45]. This higher peak magnetization observed is attributable to our fabrication technique, which produces nanocrystals that are completely free of oxide. Oxidation of the gadolinium dramatically reduces the magnetic moment, as seen in the data before hydrogen reduction (Figure 2.7, blue triangles, ▲), which results in a much lower peak magnetization value of 126 emu/g Gd. Magnetization measurements at 2 K for 120 nm and 80 nm diameter particles yielded peak magnetizations of 188 emu/g and 183 emu/g, respectively. This

decrease is attributable to the different contributions of surface and core electron magnetic moments to the total magnetization. The contribution from surface magnetism is weaker than that from core electrons. As the particle size decreases, the ratio of surface electrons to core electrons per particle increases. Consequently, the core electrons' contribution to the total magnetization is lower, which in turn, leads to a decrease in the peak magnetization. At room temperature, we observe a paramagnetic state with no detectable hysteresis. Our room-temperature peak magnetization value (5 T), 9 emu/g, also stands as the highest room temperature value reported to date. We further developed another method of increasing saturation magnetizations at the room temperature by modifying the crystalline structure of the Gd layer which will be discussed in detail in Chapter 3.

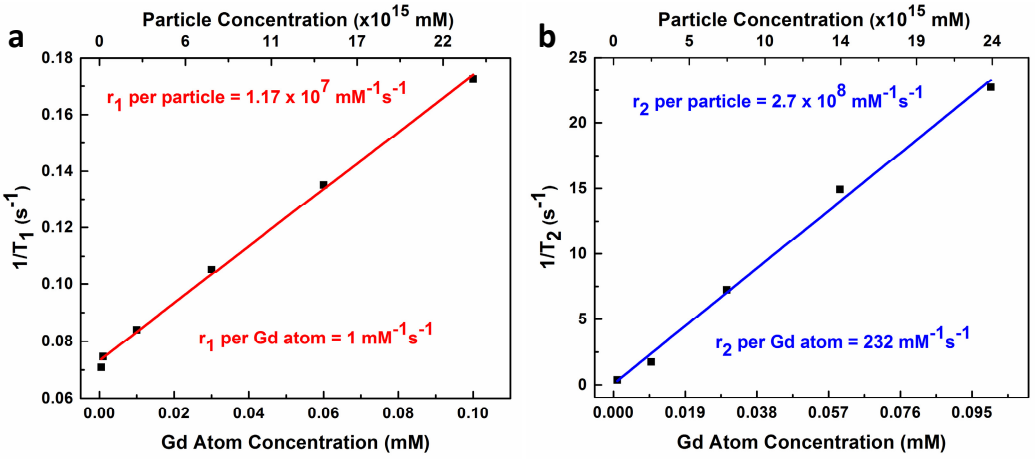

Figure 2.8: NMR $1/T_1$ and $1/T_2$

NMR relaxation rates $1/T_1$ and T_2 as function of nanoparticle concentration in aqueous solution. The concentrations are stated on a per Gd atom basis. The slopes of these graphs give relaxivity values: a) r_1 is 1.01 $\pm$ 0.02 $\mathrm{mM^{-1}s^{-1}}$ and b) r_2 is 232 $\pm$ 7 $\mathrm{mM^{-1}s^{-1}}$.

Next, we investigated the potential role of the 80 nm diameter nanoconstructs as MRI contrast agents by measuring the proton NMR relaxivities in aqueous solution. The ^{1}H NMR relaxation rates are proportional to the square of the magnetic

moment of the particles and reflect static and dynamical aspects of particles in solution. The NMR instrument (Varian 400 MHz equipped with microimaging capabilities and VNMRJ software version 4.0) used an external field of 9.4 T. To reduce the effects of radiation damping in our ^{1}H NMR experiments, the water resonance in D_2O solvent (99.8% purity) was probed instead of pure water. The proton T_1 and T_2 values, as measured using inversion-recovery and Carr-Purcell Meiboom-Gill sequences, were 14.7 s and 3.5 s, respectively. The results are shown in Figure 2.8. From the slopes of these plots, we found the r_1 and r_2 relaxivities to be 1.01 $mM^{-1}s^{-1}$ and 232.06 $mM^{-1}s^{-1}$ per Gd atom, respectively. The corresponding per-particle r_1 relaxivity was found to be 1.17 x 10^7 $mM^{-1}s^{-1}$, which is comparable to previously reported per-particle r_1 relaxivities [55, 56] where Gd^{3+} ions are loaded in nanocontainers. The r_2 value per Gd atom is more than two times higher than that of the FDA approved, state-of-the-art T_2 MRI contrast agent, Feridex, which has r_2 of 110 $mM^{-1}s^{-1}$. Compared to the newer gadolinium oxide T_2 contrast agents (for example, the Gd_2O_3 nanoparticles in [24] have an r_1 value of 10.5 $mM^{-1}s^{-1}$ per Gd atom), our r_2 values per Gd atom are more than 20 times higher. This is likely due to the larger magnetic moment. Thus, our particles are excellent T_2 contrast agents whether r_2 is measured on a per Gd atom basis or on a per-particle basis. The per-particle relaxivity (r_2 = 2.9 x 10^8 $mM^{-1}s^{-1}$) stands as the highest per-particle r_2 relaxivity reported for any T_2 contrast agents to date. Previously, the highest per-particle r_2 relaxivity was reported in [47] for Au-capped Co nanoparticles. The fact that our Gd nanoparticles act as T_2 rather than T_1 contrast agents is explained by static moment contributions that arise from particle size effects. The high-frequency (400 MHz) components of fluctuating magnetic fields that mediate T_1 relaxation processes are ineffective.

Although the nanoparticles display highly preferred properties in terms of NMR relaxation and magnetic measurements, their dispersion in aqueous media has been limited due to their ligand-free surface. In majority of the chemical syn-

thesis methods, the decoration of the particle surface with ligands happens while the nanoparticle is formed through nucleation process. However, our method which is based on nanofabrication yields nanoparticles with bare surfaces meaning that the surface functionalization needs to be performed after the particle formation. Without surface treatment, our particles start to agglomerate in water solution in less than a few minutes. As it is well known that for bio-applications, nanoparticles need to be water dispersable and this is achieved by functionalizing their surfaces with proper water friendly chemical molecules (ligands).

Functional groups can be introduced on silica surfaces through co-condensation, where a silane of interest is added in addition to the silica precursor and surfactant. Base-catalyzed hydrolysis and condensation of the silanes to form Si-O-Si bonds can be done and the chemical modification will be in the framework of the particle (Figure 2.9). Due to their high surface area and availability of hydroxyl groups on their surface, silica surfaces can be chemically modified on their surface after synthesis as well using a variety of functional groups. One common method is post-synthetic grafting. For the functionalization of the nanoparticles, a post-synthetic grafting approach was used [57]. In this approach, unfunctionalized silica surfaces are subjected to silanes that bear functional groups (such as polyethylene glycol, PEG) and that exhibit reactivity towards the free silanol groups present at the silica surface (e.g., through alkoxy groups or halide substituents of the silanes). The reaction of the silanes with the silanols through a SN reaction results in a covalently attachment of the functionalized groups to the silica surface. To avoid hydrolysis and self-condensation of the employed functional silanes, the reaction should be carried out under a dry atmosphere of an inert gas (nitrogen or argon) and in an anhydrous solvent (typically dry toluene).

We decided to decorate the silica surface with PEG because the addition of PEG to nanoparticles reduces the reticuloendothelial system uptake in *in vivo* applications and increases circulation time versus uncoated counterparts, decreases

aggregation owing to passivated surfaces, association with non-targeted serum and tissue proteins is diminished, resulting in so-called 'stealth' behavior [58]. The PEG chains reduce the charge-based contact typical of proteins and small-molecule interactions. Solubility in buffer and serum increases due to the hydrophilic ethylene glycol repeats. PEG is also biocompatible, inexpensive, versatile and FDA approved for many applications.

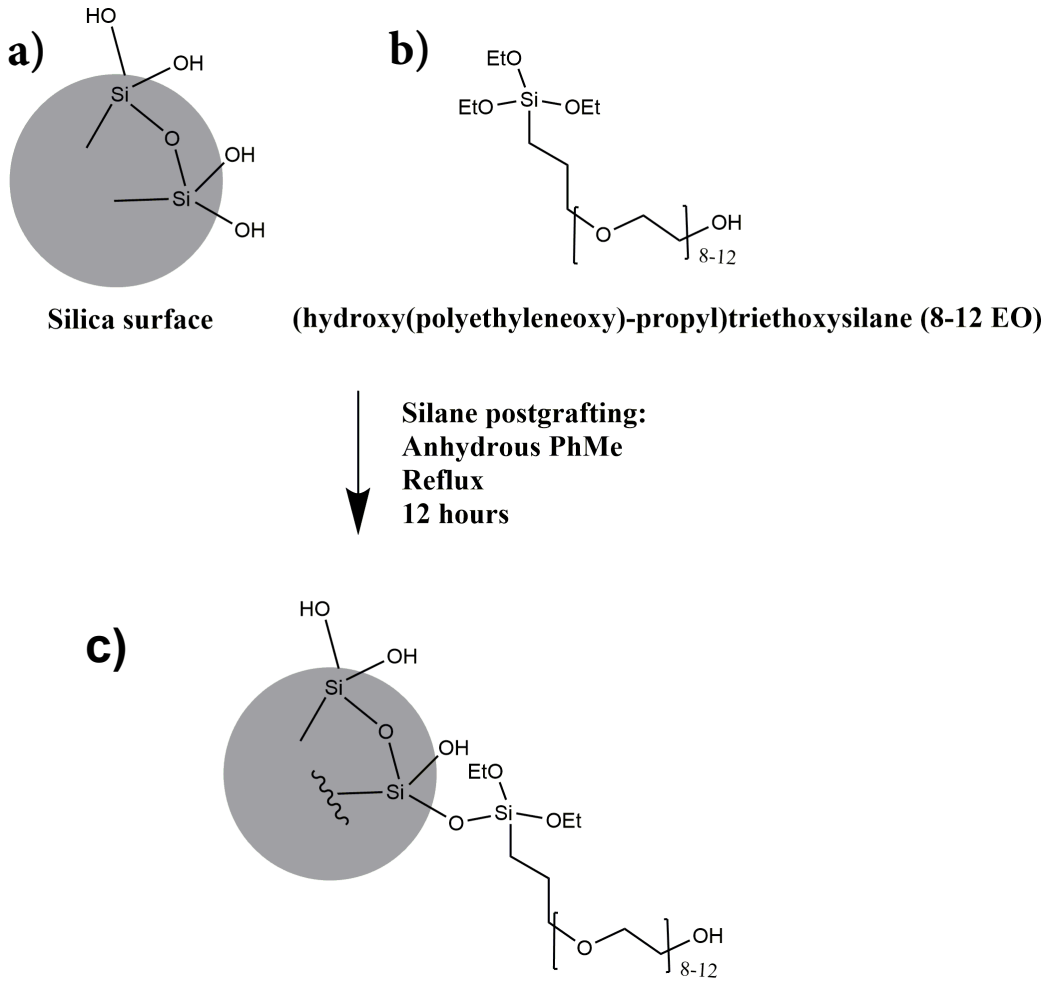

Figure 2.9: PEGylation process

a) The shell layers of the nanoparticles are silica terminated with reactive OH groups. b) The PEG precursor, (Hydroxy(polyethyleneoxy)-propyl)triethoxysilane with 8 to 12 repetition units is used. Its ethoxy terminated side involves in the reaction with OH groups of the

silica surface. c) After the PEGylation process, Si-O-Si bonds have been forms which link the PEG ligand with the silica surface.

In our approach, unfunctionalized Gd@SiO_2 nanoparticles were washed 2x with anhydrous toluene (freshly distilled from CaH_2 under an inert atmosphere of dry nitrogen) through centrifugation (10 min @ 15000 rpm using a desktop centrifugation machine) and then dispersed in a glass flask containing 10 mL of anhydrous toluene. At this point, the structure of the particles are given in Figure 2.9a where silica surface is terminated with reactive OH groups. Throughout the reaction steps, oven dried glassware is used. Then, a solution of (Hydroxy(polyethyleneoxy)-propyl)triethoxysilane with 8 to 12 repetition in ethanol (50%)(Figure 2.9b) was added, and the resulting mixture was heated to reflux while stirring under an inert atmosphere of dry nitrogen overnight (Schlenk-line techniques). Afterwards, the particles were separated by centrifugation (10 min @ 15000 rpm), washed 2x with toluene and 2x with ethanol, and redispersed in water. The end product structure is seen in Figure 2.9c where silica surface is connected to the PEG through strong Si-O-Si bond.

Figure 2.10 depicts the effect of PEGylation on the nanoparticle properties. Dynamic light scattering is used to measure the effective size of the nanoparticles where PEG addition increased the hydrodynamic diameter. This is reasonable as PEG molecules 'screen' the water molecules to some degree. Figure 2.10a shows that there is some small amount of higher size particles before the surface functionalization step which are probably aggregates of the nanoparticles. This could have happened because of not sonicating the solution long enough. PEG addition also increased the effective size of this aggregate, meaning that PEGylation worked for the aggregates as well, besides peak at larger sizes gets less intense which refers to lesser agglomeration.Figure 2.10b shows the zeta potential before and after the ligand attachment. Because the PEG precursor is relatively neutral,

zeta potential does not change much after the coating.

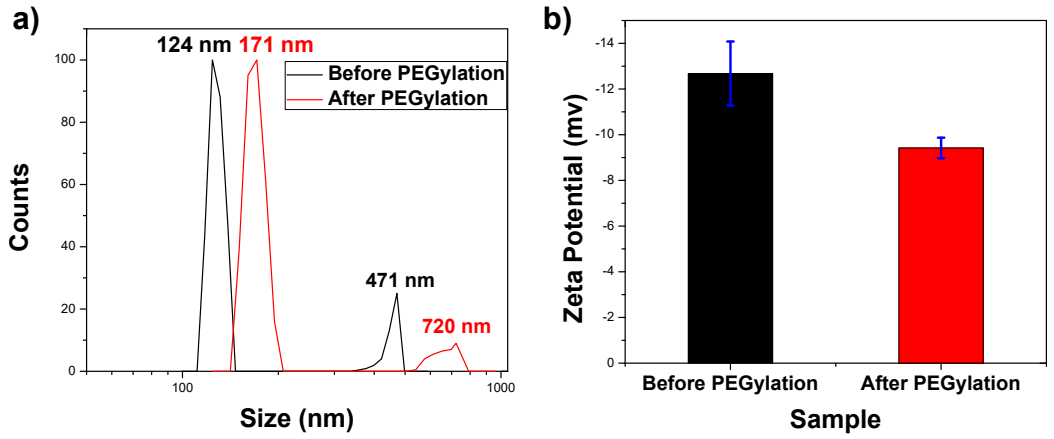

Figure 2.10: Dynamic light scattering and Zeta potential results

a) Dynamic light scattering show that after PEGylation process, the hydrodynamic diameter increases. b) Zeta potential does not change much with the addition of PEG ligands.

2.3 Conclusions

In conclusion, we developed a novel nanofabrication approach based on nanosphere lithography and metal reduction process to produce oxide-free, stable gadolinium nanocrystals with unprecedented large magnetic moments. Various sizes of nanocrystals have been realized to illustrate the flexibility of the fabrication method. For all sizes, highly monodisperse ($< 5\%$) behavior was observed. The nanocrystals were polycrystalline within the Gd core and amorphous within the silica shell. The highest magnetization to date was obtained for Gd, 206 emu/g Gd at 2 K. We also tested the potential use of these nanocrystals for magnetic resonance imaging by measuring NMR relaxivities and found a per particle transverse relaxivity value (r_2) of 2.7 x 10^8 $\mathrm{mM^{-1}s^{-1}}$, which is the highest per-particle r_2 relaxivity reported for any T_2 contrast agent to date. This high relaxivity value could be a result of the sharp features in the particles' shape. By altering the particle size and shape, higher relaxivity values may be possible. Unlike traditional

approaches, this process can further be modified to produce oxide-free nanoconstructs of other lanthanides, making them accessible for related applications.

CHAPTER 3

Controlled Nanocrystallinity in Gd Nanobowls Leads to Magnetization of 226 emu/g

Due to its unique high magnetic moment (268 emu/g at cryogenic temperatures) and high Curie temperature (293 K) Gd metal has been the subject of considerable interest over the past decade [59]. The magnetism of Gd arises from the presence of seven unpaired $4f$ electrons and magnetocrystalline anisotropy [60]. The magnetic properties of Gd display different characteristics than the standard ferromagnetic $3d$ metals such as Fe and Co [60]. Contrary to non-localized spins in $3d$ metals, $4f$ spins are indirectly coupled via the Ruderman-Kittel-Kasuya-Yosida interaction and strongly localized [61], which brings unique magnetic behavior to Gd at the nanoscale. In recent years Gd nanoparticles have found uses in magnetocaloric refrigeration [32], neutron-capture therapy [25], temperature sensing [31] and MRI [62]. Previous studies investigated the fabrication and characterization of thin films [63], multilayers [64] and nanostructures [65–67] of Gd. In more recent work, oxide-free Gd nanoparticles have been developed. Up until this work, the primary chemical synthesis methods for Gd resulted in the formation of oxides due to the aggressively reactive nature of Gd towards oxygen in ambient air. The applications and uses of Gd have thus been drastically hampered, thereby limiting our ability to probe the physical and material properties of Gd in nanoparticle form. The magnetization of Gd thin films is notably different than that of bulk crystals due to the granular structure, size and shape-related effects [59]. Nanoparticles of Gd are also expected to possess different magnetic properties than the

thin films [68]. Therefore, there is a need to produce oxide-free Gd nanoparticles and study their physical properties in nanoparticle form.

Several techniques [38–43] have been developed and applied to obtain nanoparticles and nanoscale powders of Gd, including alkalide reduction, gas-phase, arc-discharge as well as the use of multilayer precursors. Such nanoparticles were not stable in ambient air, resulting in oxides of Gd. However, oxides of Gd possess inferior magnetic properties, making them unsuitable for studies of Gd in nanoparticle form [69]. We have recently proposed a novel approach based on a nanofabrication process to produce oxide-free stable Gd nanoparticles whereby a core-shell Gd nanoparticle structure is obtained [62]. The Gd core is grown by deposition of Gd metal under high vacuum conditions whereas the shell layer provides the appropriate capping of the core, preventing oxidation. While this process managed to achieve the highest magnetizations for Gd nanoparticles to date, further optimization of the experimental conditions are possible.

To put our work in context, Table 3.1 compares the magnetization of our nanobowls to those of other Gd nanostructures and thin films previously published in the literature. The first general observation is that nanoparticles of Gd generally yield low magnetization values, whereas thin films are closer to bulk values. This is likely a consequence of greater surface effects in nanoparticles. Our nanoparticles exhibit magnetization values that are much closer to the bulk value of Gd compared to other nanoparticle synthesis methods. This is likely due to the oxide-free nature of our fabrication process [62]. In a previous study, it has been claimed that chemical synthesis could achieve oxide-free Gd nanoparticles [45]. However, these nanoparticles may not be exactly oxide-free, as evidenced by the larger magnetizations obtained here via our nanofabrication approach. When constructing this table, we have converted reported magnetization values to emu/g units to enable direct comparison, using the textbook density value of 7.90 g/cm^3 for gadolinium and the unit conversion factor 1 T = 4π x 10^{-4} emu/cm^3.

Table 3.1: Comparison of magnetization values for Gd nanostructures and thin films obtained in previous studies.

Reference	Type of Gd structure	Magnetization, as reported	Magnetization in emu/g
this study	nanoparticle	226.4 emu/g	226.4 emu/g
[59]	thin film	2.6T	261.9 emu/g
[64]	thin film	1,900 emu/cm^3	240.5 emu/g
[69]	nanorod	460 emu/cm^3	58.2 emu/g
[70]	bulk	268.4 emu/g	268.4 emu/g
[45]	nanoparticle	156 emu/g	156 emu/g
[71]	thin film	640 emu/cm^3	81 emu/g

The main conclusion of this study is the report of the highest saturation magnetization (226.4 emu/g at 2 K) for Gd nanoparticles observed to date. This was obtained through the selection of deposition rate during the nanofabrication process. The deposition rate of the Gd metal resulted in different relative composition of fcc to hcp phases within the construct. This, in turn, correlated with the magnetic properties. Deposition rate during e-beam evaporation may offer a control parameter for nanoparticle properties.

3.1 Experimental Detail

The nanoparticles were prepared using a nanolithography fabrication process whereby monolayers of polystyrene nanospheres are used as templating pattern for material deposition. Two-inch p-type $< 100 >$ silicon wafers were spin-coated with a monolayer of polystyrene nanobeads of 200 nm diameter (PS200NM Magsphere Inc., CA). The nanosphere solution was diluted with 1:1 (v/v) methanol solution to facilitate the spreading of the nanospheres on the wafer substrates for a more uniform coating and higher surface coverage. Wafers were also treated by O_2 plasma for 1 min. with a plasma power of 100 W and O_2 flow of 50 sccm before the nanobead coating step to render the wafer surface hydrophilic, enabling the nanosphere solution to better disperse on the surface. Untreated wafers were

found to have limited nanobead coverage with multilayer regions after the coating process. Oxygen reactive ion etching (RIE) was performed to reduce the size of the polymer nanospheres. By adjusting the duration and/or plasma power of this step, specific nanosphere sizes could be achieved. However, prolonged etching should be avoided as it eventually results in a loss of spherical shape. Process parameters were adjusted to obtain 100 nm size spheres with proper spherical shapes, as verified by scanning electron microscopy (SEM). Layers of 10 nm of SiO_2, 10 nm of Gd of 99.95 % purity, and 20 nm of SiO_2 layers were respectively deposited by electron-beam evaporation onto the 15° tilted substrates under high vacuum ($< 10^{-6}$ mtorr) to create Gd@SiO_2 layers onto the etched nanospheres. During the coating process, the wafer holder was rotated continuously at 30 rpm to ensure layer uniformity. Deposition rates and film thickness were controlled in real time using quartz crystal monitoring. Transmission electron microscopy (TEM) was used to confirm the film thicknesses. Prior to deposition of the Gd layer, oxygen content in the vacuum chamber was minimized by pre-depositing the Gd metal while keeping the shutter closed. This further decreases the pressure by absorbing the residual oxygen molecules in the vacuum chamber. Following the deposition of silica and Gd metal layers, the wafer substrates were sonicated in a toluene suspension to etch away the polymer beads, leaving the Gd@SiO_2 nanostructures freely suspended in solution. The nanostructures were then collected by multiple centrifugation steps and suspended in ethanol for future use.

The morphology of the nanostructures was imaged using SEM (JEOL JSM 7500F) and TEM (FEI CM120). High-resolution TEM (HRTEM, FEI Titan S/TEM) operated at 300 kV was used to image the nanolayer compositions. The crystal structures were characterized from powder samples using an X-ray diffractometer (XRD, Bruker D8 Discover Powder X-ray Diffractometer). The HRTEM samples were prepared using a FEI Nova 600 dual-beam SEM/FIB (scanning electron microscope/focused ion beam) system. Magnetic property measurements

were conducted using a Quantum Design MPMS XL superconducting quantum interference device (SQuID) magnetometer with applied field strengths of up to $\mu_0 H = 5T$. Magnetization measurements at 5 T are referred to as "saturation magnetization" because although Gd is still not completely saturated at 5 T, previous studies showed that further increases in the applied magnetic field does not lead to a significant increase in the magnetization for the commonly available laboratory field strengths. The magnetization data were corrected for the diamagnetic response of the sample holder and other background contributions.

3.2 Results and Discussion

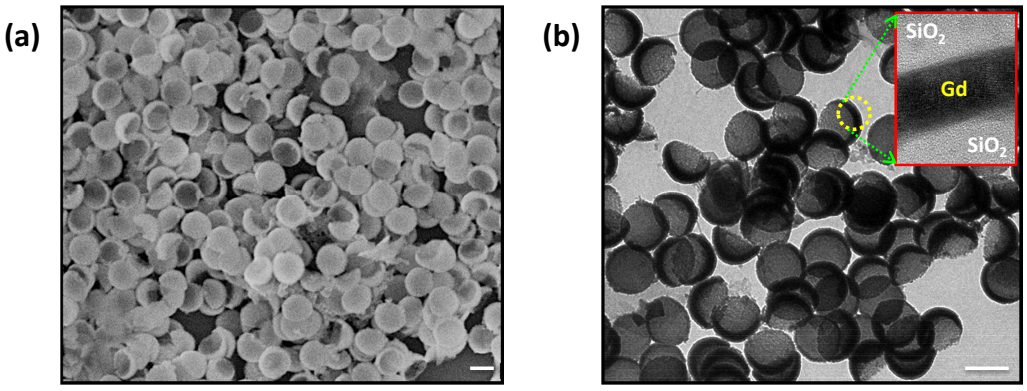

Figure 3.1: SEM and TEM of nanobowls

a) SEM and b) TEM images of the nanobowls. Scale bars, 100 nm. The inset image in (b) shows the Gd core and silica shell layers as obtained from HRTEM measurements.

Figure 3.1a shows an SEM image of the nanoparticles depicting their bowl-shaped structures. The TEM image in Figure 3.1b reveals the core-shell type structure of the particles where the light gray layer corresponds to the capping SiO_2 layer and the darker shades represent the Gd layer located in the core of the nanoconstruct (middle layer). The inset in Figure 3.1b shows the Gd and SiO_2 layers. The Gd layer was polycrystalline whereas no crystallinity was observed

for the silica layer. Both SEM and TEM images confirmed the narrow size distribution of the nanoparticles, which is a direct consequence of the controllable nanofabrication approach employed here.

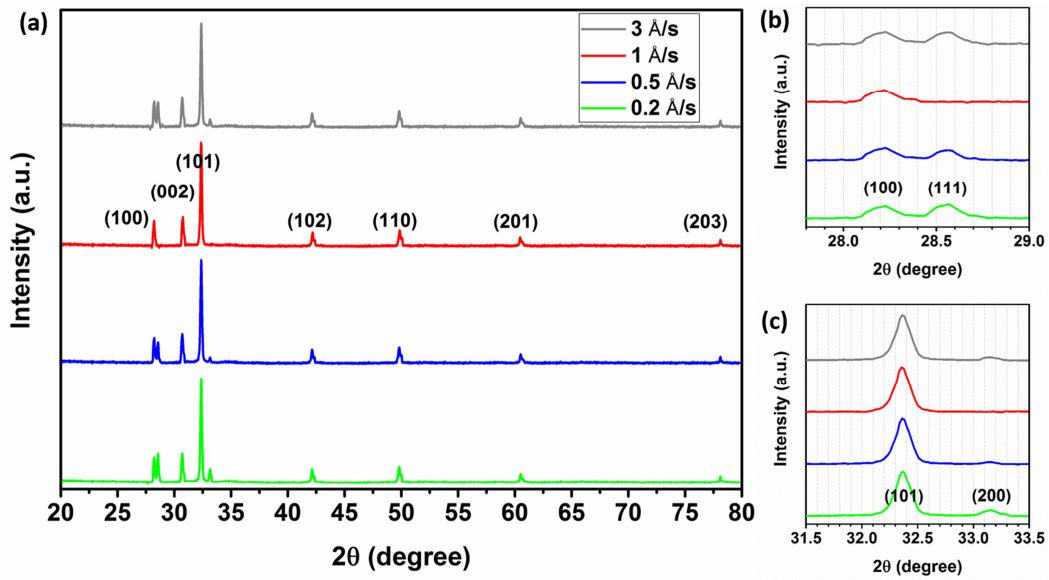

Figure 3.2: X-ray diffraction results

a) XRD spectra of the Gd nanoparticles for varying Gd deposition rates (r) of 0.2 Å/s, 0.5 Å/s, 1 Å/s and 3 Å/s, b) XRD spectra for $27.8° < 2\Theta < 29.0°$, c) XRD spectra for $31.5° < 2\Theta < 33.5°$.

Crystal structure analysis was done at room temperature using Θ-2Θ scans. The shape and width of the XRD spectra peaks were determined using the Rietveld refinement technique. The XRD patterns in Fig. 3.2a reveal that all samples are polycrystalline. A peak analysis reveals the predominance of hcp (hexagonal close-packed) phase of Gd in the samples (JCPDS: 65-0372). A second, smaller, metastable face-centered cubic (fcc), Gd phase (JCPDS: 65-8099) was also observed with a $=(5.35 \pm 0.02)$ Å. Such an fcc phase for Gd was also reported previously [44,59,67,69,72–74] for the case of Gd thin films, nanoparticles,

and nanostructures. The fcc peaks were observed at $2\Theta = 28.6°$ and $2\Theta = 33.2°$, referring to (111) and (200) planes, respectively. The highest intensity peak is associated with the hcp (101) orientation at $2\Theta = 32.3°$. We also note that there are no detectable reflections originating from oxide or hydride phases, indicating that the Gd nanoparticles are stable as a result of the protective silica shell coating.

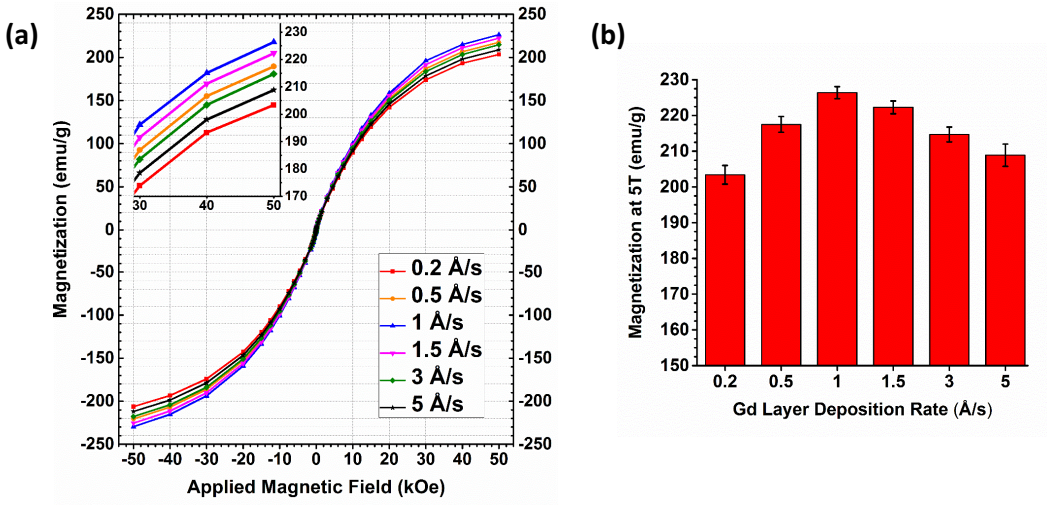

Figure 3.3: M-H vs Gd deposition rate

a) Magnetization measurements for different Gd deposition rates. Field-dependent magnetization curves indicate a trend towards saturation in magnetization at high magnetic fields (5 T). The top left inset shows that saturation magnetization peaks at deposition rate = 1 Å/s, reaching 226.4 emu/g whereas it dips at deposition rate = 0.2 Å/s, decreasing to 203.4 emu/g. The bottom left inset reveals hysteresis associated with ferromagnetism, b) Saturation magnetization versus deposition rate of Gd layer. Error bars indicate the variation of Ms obtained from 5 separate runs for each set of deposition parameters. M_s peaks at 1 Å/s, reaching 226.4 emu/g and decays as the rate goes further on both sides of 1 Å/s.

During the coating process, a deposition rate (r) of r = 0.2 Å/s was used for the Gd layer (green spectrum in Figure 3.2). This sample contains both hcp and fcc phases. When the Gd deposition rate was increased to r = 0.5 Å/s

(blue spectrum), the fcc peak intensities both for (111) and (200) were diminished compared to the r = 0.2 Å/s case (Figures 3.2b,c) whereas the hcp peaks remained unaffected. Therefore, the deposition rate affects the crystallinity of the samples. By controlling the deposition rate, different crystalline compositions could be formed. Scheunert et. al. [73], who studied hcp phase formation in thin films, found up to 2% hcp phase content and identified lattice size distortion and strain as being modulated by the deposition conditions.

Figure 3.3a shows the magnetization measurements for samples prepared using different Gd deposition rates. For the sample with r = 0.2 Å/s, the saturation magnetization (M_s) was 203.4 emu/g, whereas it jumped up to 217.5 emu/g for r = 0.5 Å/s. The latter is associated with a significantly fcc content (see Figure 3.2) lower than the r = 0.2 Å/s sample. The majority of earlier reports [67,69,72] on the magnetic properties of the Gd fcc phase found the fcc phase to be paramagnetic compared to the ferromagnetic hcp phase. However, Bertelli et. al. recently reported [71] that a ferromagnetic fcc phase could exist for 10 nm-thick Gd thin films buffered with a Ta layer. Yet, the magnetization of this fcc phase ($\sim$ 175 emu/cm^3 at 60 K) was found to be lower than that of hcp ($\sim$ 640 emu/cm^3 at 60 K). This suggests that magnetization in nanoparticles could be increased by growing particles with minimal fcc and maximal hcp content.

To investigate the possibility of optimization, we prepared samples with varying Gd deposition rates of r = 0.2 Å/s, 0.5 Å/s, 1 Å/s, 1.5 Å/s, 3 Å/s and 5 Å/s. As the deposition rate increased from 0.2 Å/s to 1 Å/s, we observed a steady increase in M_s. However, this trend is reversed beyond r = 1 Å/s, where M_s begins to decrease, reaching 208.9 emu/g for r = 5 Å/s (Figure 3.3a). A saturation value of 226.4 emu/g was achieved at r = 1 Å/s which displayed no detectable presence of fcc phase (see XRD measurements, Figures 3.2a,b,c). Figure 3.2b,c shows that the (111) and (200) fcc peaks are stronger for r = 0.2 Å/s than they are for r = 3 Å/s, which should result in a higher Ms value for the latter. For these two rates,

the Ms values are 203.4 emu/g and 214.7 emu/g, respectively.

The magnetization measurements of Figure 3.3a were recorded for applied fields in the range 5 T to 5 T. Standard ferromagnetic behavior with hysteresis is observed for all cases even though XRD spectra indicates some fcc contributions are present in most of the samples. The presence of the ferromagnetic hcp phase in all our samples is consistent with the observation of magnetic hysteresis. The presence of a small amount of paramagnetic fcc phase in the samples is reflected in the magnetic measurements as far as its effect is to decrease the saturation magnetization. The saturation magnetization of the fcc phase of Gd has been shown to be approximately 4 times less than that of hcp Gd ($\sim$ 175 emu/cm^3 vs. $\sim$ 640 emu/cm^3 at 60 K) according to Bertelli et. al. [71] From the XRD data we compute s, the ratio between the area under the strongest Bragg peaks of the hcp (101) and fcc (200) phases, defined as s = A_{fcc} / A_{hcp} (%). For the sample with lowest magnetization (r = 0.2 Å/s), s was found to be 12.2 %, whereas for the optimal condition (highest M_s, r = Å/s), s approaches zero as the fcc peaks were no longer detectable, buried in the noise. These results are shown in Table 3.2 for different deposition rates. We note the inverse correlation between s and Ms. We calculate the expected value of M_s values based on the measured Ms value for fcc Gd [75] as a weighted average of fcc and hcp fractions according to the following equation :

$$\text{expected } M_s = (226.4)(1-s) + \left(\frac{226.4}{4}\right)(s) \tag{3.1}$$

where s is a number between 0 and 1 (expressed as a percentage in Table 3.2) and 226.4/4 is the M_s value for fcc Gd from [71]. The expected values of M_s are close to the observed values (Table 3.2). Thus, we conclude that the observed decreases in saturation magnetization values at different deposition rates can be accounted for by the less magnetic fcc fraction.

To check that the observed changes in M_s are not due to random errors or

Table 3.2: Crystalline phase composition and corresponding magnetization values for Gd nanobowls fabricated using different Gd deposition rates.

Gd deposition rate (Å/s)	Area fcc (a.u.)	Area hcp (a.u.)	s factor (%)	Expected M_s (emu/g)	Observed M_s (emu/g)
0.2	57.4	469.1	12.2%	205.7	203.4
0.5	19.2	468.7	4.1%	219.4	217.5
1	∼0	469.4	∼0%	226.4	226.4
3	30.8	471.7	6.5%	215.4	214.7

other effects, error bars were obtained by repeating the experiments on different days using the same nominal parameters. Figure 3.3b shows the saturation magnetization values for different Gd deposition rates and the corresponding error bars for each case, which represent 5 different measurements. It is seen that the statistical fluctuations in magnetization values (for example, $M_s = 226.4 \pm 1.7$ emu/g for r = 1 Å/s) are lower than the observed changes in M_s. Thus, random errors do not account for the observed trends in Figure 3.3b. We conclude that the deposition rate has a direct effect on the observed magnetization values.

The lowest saturation magnetization value was found at the lowest deposition rate (r = 0.2 Å/s), where the highest content of fcc phase was measured. The presence of the fcc phase could lead to a significant contribution of intergrain and intragrain anisotropies [59]. The highest saturation magnetization we obtained was 226.4 emu/g (at 2 K), which is lower than the theoretical maximum (268 emu/g) but higher than any other Gd nanoparticles produced to date. The difference from the bulk value may be due to interfacial effects [72, 76] present in nanostructures. There have been several reports [59,73] of Gd thin films preferring to nucleate at a seed boundary in a paramagnetic fcc phase. Since the substrate (curved surface of amorphous silica here) affects the growth, other choices of geometries and materials such as Mn, Pd, Cr or W would be expected to lead to different magnetic properties [77]. The polycrystalline nature of the samples, randomly grain formations [43, 65, 66, 73, 76], crystal defects [66] and stress [43, 59, 73]

likely act as barriers to achieving high magnetism by distorting the magnetization uniformity.

3.3 Conclusions

In summary, we have applied a nanofabrication approach to prepare air stable core-shell Gd nanoparticles with high magnetic moments. Crystallinity of the nanoparticles played an important role in maximizing magnetization. The ferromagnetic hcp phase of Gd was the main dominant crystal structure whereas small amounts of paramagnetic fcc phase could be detected. We have experimentally shown that lower fcc content leads to higher saturation magnetization. We found that by adjusting the deposition rate of Gd, it is possible to control the amount of fcc content in the lattice. A deposition rate of 1 Å/s led to the highest magnetic moment of 226.4 emu/g for Gd. Such a high magnetization has never been observed experimentally to date for Gd nanoparticles. Stability of the nanoparticles along with their high magnetizations could give rise to new applications for Gd which have not been possible so far due to oxidation problems in ambient air.

CHAPTER 4

Conclusions and Future Directions

The research presented in this dissertation is focused on development of high quality MRI contrast agents based on Gd nanoparticles. In order to realize this motive, a novel nanofabrication method has been developed which requires generation of a monolayer polystyrene spheres on a substrate such as silicon wafer. The nanospheres act as sacrificial templates during the electron beam deposition steps. Tilting of the substrate at a certain degree during the deposition yields nanowbowl shaped metal coatings on top of the nanospheres. These nanospheres are removed by sonication in an organic solvent such as toluene or NMP. The end product which is the core-shell Gd@SiO_2 nanobowls are further subjected to PEGylation steps in order to make the nanoparticles water dispersable. The contrast agent needs to be water soluble and avoid agglomeration. PEG ligand renders the nanoparticles soluble in water. We have also shown that different sizes of particles with narrow size distribution ($< 5\%$) could be produced. The nanoconstructs exhibit great magnetic properties such as high saturation magnetization and increased r_2 relaxivities. Specifically, the r_2 relaxivity per particle was found to be 2.7 x 10^8 $mM^{-1}s^{-1}$ which corresponds to the highest per particle r_2 relaxivity.

Later, we found a connection between the Gd saturation magnetization and the crystallinity of the structure. The crystal structure of the nanoparticle could be altered with changing the Gd deposition rate during the nanofabrication steps. The paramagnetic fcc phase was found to be less magnetic then the ferromagnetic hcp phase. Therefore, we worked on an approach where the fcc phase is removed

and only hcp peaks are observed in XRD measurements. By doing this, we were able to even enhance the saturation magnetization of the nanoparticles. While the effect of deposition rate on the crystallinity is observed in thin film studies, it was shown in the nanoparticles for the first time by this study. We believe our work will serve as a building block for the future studies in this field.

The method we developed is of high importance for producing nanoparticles using nanofabrication techniques. The method is not only able to produce oxide-free highly magnetic Gd core and silica shell nanostructures, but also can enable the production of many other lanthanides and metals, alloys in nanoscale. For instance, Gd in our study can easily be replaced with Fe, Co, Dy or FeCo alloys and core-shell structure of the corresponding magnetic nanoparticles would be produced. Using standard wet chemistry methods, achieving this is cumbersome and requires many reaction conditions to be met. Besides, our technique allows the production of different inner and outer shell materials, which is quite limited in synthetic chemistry approaches. It is straightforward to generate SiO_2-Fe-Au core-shell nanostructures as it only requires the deposition sources of the mentioned materials. In this case, the silica shell could be functionalized with different targeting moieties whereas the silica gold can serve for different purposes such as plasmonics or imaging.

We believe this dissertation presents critical knowledge and data for the future studies in nanoparticle synthesis and the field of MRI contrast agents.

References

[1] M. Bottrill, L. Kwok, and N. J. Long. Synthesis of gd_2o_3 nanoparticles for mri contrast agents. *Chemical Society Reviews*, 35:557–571, 2006.

[2] J. P. Hornak. *The basics of NMR*. Rochester Institute of Technology, 1999.

[3] R. Weissleder. Molecular imaging in cancer. *Science*, 312(5777):1168–1171, 2006.

[4] H. R. Edward. *Breast MRI*. Springer, 2008.

[5] G. M. Lanza, P. M. Winter, S. D. Caruthers, M. S. Hughes, G. Hu, A. H. Schmieder, and S. A. Wickline. Theragnostics for tumor and plaque angiogenesis with perfluorocarbon nanoemulsions angiogenesis. *Angiogenesis*, 13(2):189–202, 2010.

[6] R. R. Edelman and S. Warach. Magnetic resonance imaging. *The New England Journal Of Medicine*, 328:708–716, 1993.

[7] S.M. Janib, A.S. Moses, and J.A. Mackay. Imaging and drug delivery using theranostic nanoparticles. *Advanced Drug Delivery Reviews*, 162(11):1052–1063, 2010.

[8] Y. Cao, L. Xu, Y. Kuang, D. Xiong, and R. Pei. Gadolinium-based nanoscale mri contrast agents for tumor imaging. *Journal of Materials Chemistry B*, 5:3431–3461, 2017.

[9] P. Caravan. Strategies for increasing the sensitivity of gadolinium based mri contrast agents. *Advanced Drug Delivery Reviews*, 35:512–523, 2006.

[10] S. Aime, M. Botta, and E. Terreno. Gd(iii)-based contrast agents for mri. *Advances in Inorganic Chemistry*, 57:173–237, 2005.

[11] S. Aime, M. Botta, M. Fasano, and E. Terreno. Lanthanide(iii) chelates for nmr biomedical applications. *Chemical Society Reviews*, 27:19–29, 1998.

[12] T.J. Fraum, D. R. Ludwig, M. R. Bashir, and K. J. Fowler. Gadolinium-based contrast agents: A comprehensive risk assessment. *Journal of Magnetic Resonance Imaging*, 46(2):338–353, 2017.

[13] Y. Liu and N. Zhang. Gadolinium loaded nanoparticles in theranostic magnetic resonance imaging. *Biomaterials*, 33(21):5363–5375, 2012.

[14] B. D. Cullity and C. D. Graham. *Introduction to Magnetic Materials*. Wiley-IEEE Press, 2008.

[15] J.-L. Bridot, A.-C. Faure, S. Laurent, C. Riviere, C. Billotey, B. Hiba, M. Janier, V. Josserand, J.-L. Coll, L. V. Elst, R. Muller, S. Roux, P. Perriat, and O. Tillement. Hybrid gadolinium oxide nanoparticles: Multimodal contrast agents for in vivo imaging. *Journal of the American Chemical Society*, 129(16):5076–5084, 2007.

[16] N. Sakai, L. Zhu, A. Kurokawa, H. Takeuchi, S. Yano, T. Yanoh, N. Wada, S. Taira, Y. Hosokai, A. Usui, Y. Machida, H. Saito, and Y. Ichiyanagi. Synthesis of gd2o3 nanoparticles for mri contrast agents. *Journal of Physics: Conference Series*, 352(1):012008, 2012.

[17] L. Faucher, Y. Gossuin, A. Hocq, and M.-A. Fortin. Impact of agglomeration on the relaxometric properties of paramagnetic ultra-small gadolinium oxide nanoparticles. *Nanotechnology*, 22(29):295103, 2011.

[18] L. Faucher, A.-A. Guay-Begin, J. Lagueux, M.-F. Cote, E. Petitclerc, and M.-A. Fortin. Ultra-small gadolinium oxide nanoparticles to image brain cancer cells in vivo with mri. *Contrast Media and Molecular Imaging*, 6(4):209–218, 2011.

[19] A. T. M. Anishur Rahman, P. Majewski, and K. Vasilev. Gd_2o_3 nanoparticles: size-dependent nuclear magnetic resonance. *Contrast Media and Molecular Imaging*, 8(1):92–95, 2013.

[20] L. Zhou, Z. Gu, X. Liu, W. Yin, G. Tian, L. Yan, S. Jin, W. Ren, G. Xing, W. Li, X. Chang, Z. Hu, and Y. Zhao. Size-tunable synthesis of lanthanide-doped gd_2o_3 nanoparticles and their applications for optical and magnetic resonance imaging. *Journal of Materials Chemistry*, 22(3):966–974, 2012.

[21] R. Di Corato, F. Gazeau, C. Le Visage, D. Fayol, P. Levitz, F. Lux, D. Letourneur, N. Luciani, O. Tillement, and C. Wilhelm. High-resolution cellular mri: Gadolinium and iron oxide nanoparticles for in-depth dual-cell imaging of engineered tissue constructs. *ACS Nano*, 7(9):7500–7512, 2013.

[22] L. Faucher, M. Tremblay, J. Lagueux, Y. Gossuin, and M.-A. Fortin. Rapid synthesis of pegylated ultrasmall gadolinium oxide nanoparticles for cell labeling and tracking with mri. *ACS Applied Materials and Interfaces*, 4(9):4506–4515, 2012.

[23] S. Li, H. Liu, L. Li, N.-Q. Luo, R.-H. Cao, D.-H. Chen, and Y.-Z. Shao. Mesoporous silica nanoparticles encapsulating gd_2o_3 as a highly efficient magnetic resonance imaging contrast agent. *Applied Physics Letters*, 98(9):093704, 2011.

[24] J. Y. Park, M. J. Baek, E. S. Choi, S. Woo, J. H. Kim, T. J. Kim, J. C. Jung, K. S. Chae, Y. Chang, and G. H Lee. Paramagnetic ultrasmall gadolinium oxide nanoparticles as advanced t_1 mri contrast agent: Account for large

longitudinal relaxivity, optimal particle diameter, and in vivo t_1 mr images. *ACS Nano*, 3(11):3663–3669, 2009.

[25] D. C. F. Soares, M. . de B. C. Menezes, R. G. dos Santos, and G. A. Ramal-des. 159gd: preparation and preliminary evaluation as a potential antitumoral radionuclide. *Journal of Radioanalytical and Nuclear Chemistry*, 284(2):315–320, 2010.

[26] G. D. Stasio, D. Rajesh, J. M. Ford, M. J. Daniels, R. J. Erhardt, B. H. Frazer, T. Tyliszczak, M. K. Gilles, R. L. Conhaim, S. P. Howard, J. F. Fowler, F. Estve, and M. P. Mehta. Motexafin-gadolinium taken up in vitro by at least 90% of glioblastoma cell nuclei. *Clinical Cancer Research*, 12(1):206–213, 2006.

[27] T. Goorley and H. Nikjoo. Electron and photon spectra for three gadolinium-based cancer therapy approaches. *Radiation Research*, 154(5):556–563, 2000.

[28] F. Shikata, H. Tokumitsu, H. Ichikawa, and Y. Fukumori. In vitro cellular accumulation of gadolinium incorporated into chitosan nanoparticles designed for neutron-capture therapy of cancer. *European Journal of Pharmaceutics and Biopharmaceutics*, 53(1):57–63, 2002.

[29] H. Tokumitsu, J. Hiratsuka, Y. Sakurai, T. Kobayashi, H. Ichikawa, and Y. Fukumori. Gadolinium neutron-capture therapy using novel gadopentetic acid-chitosan complex nanoparticles: in vivo growth suppression of experimental melanoma solid tumor. *Cancer Letters*, 150(2):177–182, 2000.

[30] G. Le Duc, I. Miladi, C. Alric, P. Mowat, E. Bruer-Krisch, A. Bouchet, E. Khalil, C. Billotey, M. Janier, F. Lux, T. Epicier, P. Perriat, S. Roux, and O. Tillement. Toward an image-guided microbeam radiation therapy using gadolinium-based nanoparticles. *Cancer Letters*, 5(12):9566–9574, 2011.

[31] S. M. Borisov and I. Klimant. Luminescent oxygen-sensing and temperature-sensing materials based on gadolinium(iii) and europium(iii) complexes embedded in an acridonepolystyrene conjugate. *Analytical and Bioanalytical Chemistry*, 404(10):2797–2806, 2012.

[32] K. A. GschneidnerJr, V. K. Pecharsky, and A. O. Tsokol. Recent developments in magnetocaloric materials. *Analytical and Bioanalytical Chemistry*, 68(6):1479–1539, 2005.

[33] L.-X. Chang, G. Xiong, L. Wang, P. Cheng, and B. Zhao. A 24-gd nanocapsule with a large magnetocaloric effect. *Chemical Communications*, 49(11):1055–1057, 2013.

[34] F.-S. Guo, J.-D. Leng, J.-L. Liu, Z.-S. Meng, and M.-L. Tong. Polynuclear and polymeric gadolinium acetate derivatives with large magnetocaloric effect. *Inorganic Chemistry*, 51(1):405–413, 2012.

[35] V. Franco, J. S. Blzquez, B. Ingale, and A. Conde. The magnetocaloric effect and magnetic refrigeration near room temperature: Materials and models. *Annual Review of Materials Research*, 42(1):305–342, 2012.

[36] J. P. Jakubovics. *Magnetism and magnetic materials*. Cambridge University Press, 1994.

[37] M.-A. Fortin, Jr Petoral, R. M., F. Soderlind, A. Klasson, M. Engstrm, T. Veres, P.-O. Kall, and K. Uvdal. Polyethylene glycol-covered ultra-small gd2o3 nanoparticles for positive contrast at 1.5 t magnetic resonance clinical scanning. *Nanotechnology*, 18(39):395501, 2007.

[38] J. A. Nelson, L. H. Bennett, and M. J. Wagner. Solution synthesis of gadolinium nanoparticles. *Journal of American Chemical Society*, 124(12):2979–2983, 2002.

[39] P. E. Chizhov, A. N. Kostigov, and V. I. Petinov. Structure and magnetic properties of rare earth small particles. *Solid State Communications*, 42(4):323–326, 1982.

[40] Y. Z. Shao, C. H. Shek, and J. K. L. Lai. Preparation and size evaluation of nanometer gadolinium powder. *Journal of Materials Research*, 13(10):2969–2974, 1998.

[41] P. Z. Si, I. Skorvanek, J. Kovac, D. Y. Geng, X. G. Zhao, and Z. D. Zhang. Structure and magnetic properties of gd nanoparticles and carbon coated gd/gdc_2 nanocapsules. *Journal of Applied Physics*, 94(10):6779–6784, 2003.

[42] D. Michels, III Krill, C. E., and R. Birringer. Grain-size-dependent curie transition in nanocrystalline gd: The influence of interface stress. *Journal of Magnetism and Magnetic Materials*, 250(Supplement C):203–211, 2002.

[43] Z. C. Yan, Y. H. Huang, Y. Zhang, H. Okumura, J. Q. Xiao, S. Stoyanov, V. Skumryev, G. C. Hadjipanayis, and C. Nelson. Magnetic properties of gadolinium and terbium nanoparticles produced via multilayer precursors. *Physical Review B*, 67(5):054403, 2003.

[44] I. Aruna, B. R. Mehta, L. K. Malhotra, and S. M. Shivaprasad. Stability and hydrogenation of bare gadolinium nanoparticles. *Advanced Functional Materials*, 15(1):131–137, 2005.

[45] C. Yan and M. Wagner. Air- and water-stable gold-coated gadolinium metal nanocrystals. *Nano Letters*, 13(6):2611–2614, 2013.

[46] B. D. Gates, Q. Xu, M. Stewart, D. Ryan, C. G. Willson, and G. M. Whitesides. New approaches to nanofabrication: Molding, printing, and other techniques. *Chemical Reviews*, 105(4):1171–1196, 2005.

[47] L.-S. Bouchard, M. S. Anwar, G. L. Liu, B. Hann, Z. H. Xie, J. W. Gray, X. Wang, A. Pines, and F. F. Chen. Picomolar sensitivity mri and photoacoustic imaging of cobalt nanoparticles. *Proceedings of the National Academy of Sciences of the United States of America*, 106(11):4085–4089, 2009.

[48] J. C. Hulteen and R. P. Van Duyne. Nanosphere lithography: A materials general fabrication process for periodic particle array surfaces. *Journal of Vacuum Science and Technology A: Vacuum, Surfaces, and Films*, 13(3):1553–1558, 1995.

[49] C. L. Cheung, R. J. Nikolic, C. E. Reinhardt, and T. F. Wang. Fabrication of nanopillars by nanosphere lithography. *Nanotechnology*, 17(5):1339–1343, 2006.

[50] T. Asefa and Z. Tao. Biocompatibility of mesoporous silica nanoparticles. *Chemical Research in Toxicology*, 25(11):2265–2284, 2012.

[51] F. Tang, L. Li, and D. Chen. Mesoporous silica nanoparticles: Synthesis, biocompatibility and drug delivery. *Advanced Materials*, 24(12):1504–1534, 2002.

[52] T. Yu, A. Malugin, and H. Ghandehari. Impact of silica nanoparticle design on cellular toxicity and hemolytic activity. *ACS Nano*, 5(7):5717–5728, 2011.

[53] T. Hyeon. Chemical synthesis of magnetic nanoparticles. *Chemical Communi*, 8:927–934, 2003.

[54] W. Zhao, J. Gu, L. Zhang, H. Chen, and J. Shi. Fabrication of uniform magnetic nanocomposite spheres with a magnetic core/mesoporous silica shell structure. *Journal of American Chemical Society*, 127(25):8916–8917, 2005.

[55] A. M. Morawski, P. M. Winter, K. C. Crowder, S. D. Caruthers, R. W. Fuhrhop, M. J. Scott, J. D. Robertson, D. R. Abendschein, G. M. Lanza, and S. A. Wickline. Targeted nanoparticles for quantitative imaging of sparse molecular epitopes with mri. *Magnetic Resonance in Medicine*, 51(3):480–486, 2004.

[56] J. S. Ananta, B. Godin, R. Sethi, L. Moriggi, X. Liu, R. E. Serda, R. Krishnamurthy, R. Muthupillai, R. D. Bolskar, L. Helm, M. Ferrari, L. J. Wilson, and P. Decuzzi. Geometrical confinement of gadolinium-based contrast agents in nanoporous particles enhances t1 contrast. *Nature Nanotechnology*, 5(11):815–821, 2010.

[57] C. Sanchez, C. Boissiere, D. Grosso, C. Laberty, and L. Nicole. Design, synthesis, and properties of inorganic and hybrid thin films having periodically organized nanoporosity. *Chemistry of Materials*, 20(3):682–737, 2008.

[58] J. V. Jokerst, T. Lobovkina, R. N. Zare, and S. S. Gambhir. Nanoparticle pegylation for imaging and therapy. *Nanomedicine*, 6(4):715–728, 2011.

[59] G. Scheunert, W. R. Hendren, C. Ward, and R. M. Bowman. Magnetization of 2.6t in gadolinium thin films. *Applied Physics Letters*, 101(14):142407, 2012.

[60] M. Chakravorty and A. K. Raychaudhuri. Low field magnetoresistance of gadolinium nanowire. *Journal of Applied Physics*, 115(5):054308, 2014.

[61] M. A. Ruderman, , and C. Kittel. Indirect exchange coupling of nuclear magnetic moments by conduction electrons. *Physical Review*, 96(1):99–102, 1954.

[62] Y. N. Ertas, N. N. Jarenwattananon, and L.-S. Bouchard. Oxide-free gadolinium nanocrystals with large magnetic moments. *Chemistry of Materials*, 27(15):5371–5376, 2015.

[63] U. Stetter, M. Farle, K. Baberschke, and W. G. Clark. Critical behavior of strained epitaxial gd films: In situ ac-susceptibility measurements in uhv. *Physical Review B*, 45(1):503–506, 1992.

[64] J. S. Jiang and C. L. Chien. Magnetization and finitesize effects in gd/w multilayers. *Journal of Applied Physics*, 79(8):5615–5617, 1996.

[65] M. Yue, J. X. Zhang, H. Zeng, and K. Wang. Preparation, microstructure, and magnetic properties of bulk nanocrystalline gd metal. *Applied Physics Letters*, 89(23):232504, 2006.

[66] F. Dobrich, M. Elmas, A. Ferdinand, J. Markmann, M. Sharp, H. Eckerlebe, J. Kohlbrecher, R. Birringer, and A. Michels. Grain-boundary-induced spin disorder in nanocrystalline gadolinium. *Journal of Physics: Condensed Matter*, 21(15):156003, 2009.

[67] X. G. Liu, D. Y. Geng, Q. Zhang, J. J. Jiang, W. Liu, and Z. D. Zhang. Microstructure and magnetic properties of graphite-coated gd nanocapsules. *Applied Physics Letters*, 94(10):103104, 2009.

[68] M. J. O'Shea and P. Perera. Influence of nanostructure (layers and particles) on the magnetism of rare-earth materials. *Journal of Applied Physics*, 85(8):4322–4324, 1999.

[69] C. J. Hsu, S. V. Prikhodko, C. Y. Wang, L. J. Chen, and G. P. Carman. Magnetic anisotropy in nanostructured gadolinium. *Journal of Applied Physics*, 111(5):053916, 2012.

[70] H. E. Nigh, S. Legwold, and F. H. Spedding. Magnetization and electrical resistivity of gadolinium single crystals. *Physical Review*, 132(3):1092–1096, 1963.

[71] T. P. Bertelli, E. C. Passamani, C. Larica, V. P. Nascimento, A. Y. Takeuchi, and M. S. Pessoa. Ferromagnetic properties of fcc gd thin films. *Journal of Applied Physics*, 117(20):203904, 2015.

[72] G. Ward, C. and. Scheunert, W. R. Hendren, R. Hardeman, M. A. Gubbins, and R. M. Bowman. Realizing a high magnetic moment in gd/cr/feco: The role of the rare earth. *Applied Physics Letters*, 102(9):092403, 2013.

[73] G. Scheunert, C. Ward, W. R. Hendren, A. A. Lapicki, R. Hardeman, M. Mooney, M. Gubbins, and R. M. Bowman. Influence of strain and polycrystalline ordering on magnetic properties of high moment rare earth metals and alloys. *Journal of Physics D: Applied Physics*, 47(41):415005, 2014.

[74] A. E. Curzon and H. G. Chlebek. The observation of face centred cubic gd, tb, dy, ho, er and tm in the form of thin films and their oxidation. *Journal of Physics F: Metal Physics*, 3(1):1, 1973.

[75] M. Chakravorty and A. K. Raychaudhuri. Magnetoresistance of polycrystalline gadolinium with varying grain size. *Journal of Applied Physics*, 117(3):034301, 2015.

[76] S. P. Mathew and S. N. Kaul. Magnetization processes in nanocrystalline gadolinium. *Journal of Physics: Condensed Matter*, 24(25):256008, 2012.

[77] G. Scheunert, O. Heinonen, R. R. Hardeman, A. Lapicki, M. Gubbins, and R. M. Bowman. A review of high magnetic moment thin films for microscale and nanotechnology applications. *Applied Physics Reviews*, 3(1):011301, 2016.